Atmos. Chem. Phys. Discuss., 15, 24751–24803, 2015
www.atmos-chem-phys-discuss.net/15/24751/2015/
doi:10.5194/acpd-15-24751-2015

Atmospheric Chemistry and Physics Discussions

Observations of the spectral dependence of particle depolarization ratio of aerosols using NASA Langley airborne High Spectral Resolution Lidar

S. P. Burton[1], J. W. Hair[1], M. Kahnert[2,3], R. A. Ferrare[1], C. A. Hostetler[1], A. L. Cook[1], D. B. Harper[1], T. A. Berkoff[1], S. T. Seaman[1,4], J. E. Collins[1,5], M. A. Fenn[1,5], and R. R. Rogers[1,a]

[1]NASA Langley Research Center, MS 475, Hampton, VA, 23681, USA
[2]Research Department, Swedish Meteorological and Hydrological Institute, Folkborgsvägen 17, 60176 Norrköping, Sweden
[3]Department of Earth and Space Science, Chalmers University of Technology, 41296 Gothenburg, Sweden
[4]National Institute of Aerospace, 100 Exploration Way, Hampton, VA, 23666, USA
[5]Science Systems and Applications, Inc., One Enterprise Pkwy, Hampton, VA, 23666, USA
[a]now at: Lord Fairfax Community College, Middletown, VA 22645, USA

Received: 17 August 2015 – Accepted: 24 August 2015 – Published: 11 September 2015

Correspondence to: S. P. Burton (sharon.p.burton@nasa.gov)

Published by Copernicus Publications on behalf of the European Geosciences Union.

ACPD
15, 24751–24803, 2015

Abstract

Particle depolarization ratio is presented for three case studies from the NASA Langley airborne High Spectral Resolution Lidar-2 (HSRL-2). Particle depolarization ratio from lidar is an indicator of non-spherical particles and is sensitive to the fraction of non-spherical particles and their size. The HSRL-2 instrument measures depolarization at three wavelengths: 355, 532, and 1064 nm. The three measurement cases presented here include two cases of dust aerosol and one case of smoke aerosol. These cases have partial analogs in earlier HSRL-1 depolarization measurements at 532 and 1064 nm and in literature, but the availability of three wavelengths gives additional insight into different scenarios for non-spherical particles in the atmosphere. A case of transported Saharan dust has a spectral dependence with a peak of 0.30 at 532 nm with smaller particle depolarization ratios of 0.27 and 0.25 at 1064 and 355 nm, respectively. A case of locally generated wind-blown North American dust has a maximum of 0.38 at 1064 nm, decreasing to 0.37 and 0.24 at 532 and 355 nm, respectively. The cause of the maximum at 1064 nm is inferred to be very large particles that have not settled out of the dust layer. The smoke layer has the opposite spectral dependence, with the peak of 0.24 at 355 nm, decreasing to 0.09 and 0.02 at 532 and 1064 nm. The depolarization in the smoke case is inferred to be due to the presence of coated soot aggregates. We also point out implications for the upcoming EarthCARE satellite, which will measure particle depolarization ratio only at 355 nm. At 355 nm, the particle depolarization ratios for all three of our case studies are very similar, indicating that smoke and dust may be more difficult to separate with EarthCARE measurements than heretofore supposed.

ACPD
15, 24751–24803, 2015

1 Introduction

The impact of aerosols on climate depends on their horizontal and vertical distribution and microphysical properties. Lidar is an important tool for remote sensing of aerosol, because it provides vertically resolved information on aerosol abundance and aerosol type. Global lidar observations of aerosol have been provided by the Cloud-Aerosol Lidar and Infrared Pathfinder Satellite Observations (CALIPSO) satellite since 2006 (Winker et al., 2007). Another satellite lidar, the experimental Cloud-Aerosol Transport System (CATS) instrument on the International Space Station (ISS) (McGill et al., 2012) was recently launched in January 2015, and the Earth Clouds Aerosols and Radiation Explorer (EarthCARE) satellite (Illingworth et al., 2014) is due to launch in 2018. NASA Langley airborne High Spectral Resolution Lidars, HSRL-1 and HSRL-2, have participated in many process-oriented field campaigns, have provided validation and calibration data for CALIPSO since 2006 (Rogers et al., 2011, 2014), and will also be useful for validating the EarthCARE lidar measurements.

One extremely useful lidar aerosol measurement is the particle depolarization ratio, an indicator of non-spherical particles. CALIPSO particle depolarization ratio data have been used, for example, to assess the global distribution and transport of dust (e.g. Johnson et al., 2012; Liu et al., 2013; Yang et al., 2013). This measurement will also be part of the suite of measurements made by the ATLID (Atmospheric Lidar) on EarthCARE; however, CALIPSO measures depolarization at 532 nm and ATLID will measure it at 355 nm (Groß et al., 2014; Illingworth et al., 2014). Since the airborne HSRL-2 measures particle depolarization ratio at both of these wavelengths and also at 1064 nm, observations from this instrument are useful for assessing how the measurements from the two satellite instruments will correspond.

Aerosol particle depolarization ratio from lidar has long been used for the detection and assessment of dust and volcanic ash since it is a clear indicator of non-spherical particles. The particle depolarization ratio is known to be sensitive to the amount of dust or ash in a mixture (Sugimoto and Lee, 2006; Tesche et al., 2009a) and also to the size

ACPD
15, 24751–24803, 2015

of the non-spherical particles (Ansmann et al., 2009; Gasteiger and Freudenthaler, 2014; Gasteiger et al., 2011).

While a significant amount of study has been made of depolarization by dust and ash, smoke has also been observed to produce significant depolarization of lidar light in some cases (e.g. Fiebig et al., 2002; Sassen and Khvorostyanov, 2008; Sugimoto et al., 2010), but not in others (e.g. Müller et al., 2005). Even for cases with significant depolarization, the depolarization signature for smoke is generally smaller than for dust, at the wavelengths of 532 and 1064 nm where most lidar depolarization measurements of smoke have been made.

We will describe two dust cases and a smoke case where depolarizing aerosol was observed simultaneously at three wavelengths by the NASA Langley airborne HSRL-2 instrument. We show consistency between the three HSRL-2 cases and three previously published cases from the predecessor HSRL-1 instrument in which similar measurements were made at 532 and 1064 nm, and we also discuss similarities and differences with published lidar measurements globally. We find that the three cases each have a different spectral dependence of the particle depolarization ratio. Accordingly, we discuss possible explanations for these differences with reference to published studies. We also point out implications for future space-based observations of aerosol depolarization. We begin in Sect. 2 with a description of the NASA Langley airborne HSRL instruments and the methodology for depolarization measurements, including a systematic error assessment. In Sect. 3 we describe and discuss the dust cases and in Sect. 4 we describe and discuss the smoke case. We summarize the discussion and conclude in Sect. 5. In the Appendix we give more details about the estimation of systematic errors.

2 Instrument description and measurement methodology

The NASA Langley second-generation airborne High Spectral Resolution Lidar-2 (HSRL-2) uses the HSRL technique (Shipley et al., 1983) to independently measure

ACPD
15, 24751–24803, 2015

aerosol extinction and backscatter at 355 and 532 nm and the standard backscatter technique (Fernald, 1984) to measure aerosol backscatter at 1064 nm. It also measures depolarization ratio at all three wavelengths. It is a follow-on to the successful airborne HSRL-1 instrument (Hair et al., 2008), which has made measurements at 532 and 1064 nm since 2006 (Rogers et al., 2009). Data are sampled at 0.5 s temporal and 30 m vertical resolutions. Aerosol backscatter and depolarization products are averaged 10 s horizontally (~ 1 km at nominal aircraft speed) and aerosol extinction products are averaged 60 s (~ 6-km) horizontally and 150 m vertically. Besides aerosol backscatter, extinction, and depolarization ratio, products also include horizontally- and vertically-resolved curtains of backscatter Ångström exponent and extinction Ångström exponent. Operational retrievals also provide mixing ratio of nonspherical-to-spherical backscatter (Sugimoto and Lee, 2006), aerosol type and partitioning of aerosol optical depth (AOD) by type (Burton et al., 2012), aerosol mixed-layer height (Scarino et al., 2014), and aerosol microphysics for spherical particles (Müller et al., 2014). HSRL-2 has been successfully deployed from the NASA LaRC King Air B200 aircraft on four field missions since 2012 and has obtained over 350 science flight hours. The data for the case studies presented here are available on the DISCOVER-AQ (Deriving Information on Surface Conditions from Column and Vertically Resolved Observations Relevant to Air Quality) data archive at http://www-air.larc.nasa.gov/missions/discover-aq/discover-aq.html or using the data doi:10.5067/Aircraft/DISCOVER-AQ/Aerosol-TraceGas.

2.1 Depolarization optics

In this paper, we will focus on the measurements of particle depolarization ratio. Figure 1 shows a simplified diagram of the optics of the transmission system that are relevant to the measurement of depolarization. The primary optical components for the polarization of the transmitted beams are Glan Laser Polarizers, which have a very high polarization extinction ratio of $2 \times 10^5 : 1$ (i.e. the light is highly linear polarized with an extremely small fraction of cross-polarized light). The calibration of depolarization for

ACPD
15, 24751–24803, 2015

HSRL-2 is done in a manner similar to HSRL-1 (Hair et al., 2008) for all three wavelengths. The polarization axis of the outgoing light is matched to that of the receiver with an approach similar to that outlined by Alvarez et al. (2006) using seven fixed polarization angles between ±45°, using the half-wave calibration wave plates indicated in Fig. 1. Following the alignment, the gain ratio between the cross-polarized and co-polarized channels is routinely determined in flight by rotating the transmitted polarization 45° relative to the receiver, so that both channels measure equal components of the co-polarized and cross-polarized backscatter returns, in a cloud-free portion of the profile. See Hair et al. (2008) for a detailed description of the calibrations. See the caption accompanying Fig. 1 for more details of the HSRL-2 transmission optics.

The receiver optics relevant to depolarization measurements are shown in Fig. 2. The collimated light arrives from the telescope and is split into the three wavelengths using dichroic beam splitters. Each beam is then passed through an interference filter (1064 nm) or a combination of interference filter and etalon (355 and 532 nm) to remove background scattering. The effective full-width half-max (FWHM) bandwidths for the three channels are 0.4 nm (3.5 cm^{-1}) at 1064, 0.03 nm (1.1 cm^{-1}) at 532 nm, and 0.045 nm (3.6 cm^{-1}) at 355 nm. Note that these bandwidths are narrow enough to completely exclude the rotational Raman sidebands from the receiver optics, which are found starting at ±11.9 cm^{-1} for N_2 and ±14.4 cm^{-1} for O_2 (Behrendt and Nakamura, 2002). The 1064 nm channel includes a half-wave plate which can be used to correct any small polarization misalignment in the receiver system, since the 532 and 1064 nm beams are transmitted together. This half-wave plate is set during installation and is not rotated during normal operations. Next, each beam passes through Polarization Beam Splitters (PBS) to be separated into components that are co-polarized and cross-polarized with respect to the transmitted beam. Since the extinction ratio of the light exiting a PBS is greater in the transmitted direction than in the reflected direction, a second "clean-up" PBS is included for each detector wavelength to further improve the extinction ratio for the co-polarized light. The polarization extinction ratio measured in the system is 300 : 1 for the cross-polarized light at 355 nm, 431 : 1 for

ACPD
15, 24751–24803, 2015

the co-polarized light at 355 nm (with two PBS) and greater than 1000 : 1 for both polarization states at 532 and 1064 nm. After exiting the polarization optics, the light in the 1064 nm channel goes directly to the Avalanche Photodetectors (APD). The co-polarized signal and cross-polarized signal are used to determine total depolarization. As described by Hair et al. (2008) for HSRL-1, the co-polarized 532 nm channel is also split into a portion that is passed through an iodine cell leaving only molecular return and a channel with both molecular and aerosol return. At 355 nm, a portion of the co-polarized light is captured for the determination of the total depolarization, while the rest of the co-polarized light is transmitted through an interferometer to produce one channel that is dominated by the aerosol return with little signal from molecular scattering and a complementary channel that is dominated by the molecular signal with much less aerosol backscatter signal. The separation of the aerosol and molecular signals is the basis of the HSRL technique for extinction and backscatter retrieval. Since it is also relevant to the systematic error in particle depolarization ratio, it will be discussed again in Sect. 2.2, below.

The volume (or total) depolarization ratio is the ratio of the signal in the cross-polarized channel to that in the co-polarized channel, normalized by the measured gain ratio.

$$\delta_{\text{tot}} = G_{\text{dep}} \frac{P^{\perp}}{P^{\parallel}} \tag{1}$$

In Eq. (1), $P^{\parallel}$ and $P^{\perp}$ are proportional to the light measured by the photodetectors or photomultipliers in the co-polarized channel and the cross-polarized channel, respectively; G_{dep} is the electro-optical gain ratio between the two (for each wavelength) and δ^{tot} is the volume depolarization ratio, which is the ratio of the cross-polarized to co-polarized channel returns using the appropriate gain ratio.

ACPD
15, 24751–24803, 2015

The particle depolarization ratio is calculated from the volume depolarization ratio using the following:

$$\delta_a = \frac{\beta_a^{\perp}}{\beta_a^{\parallel}} = \frac{R\delta_{tot}(\delta_m + 1) - \delta_m(\delta_{tot} + 1)}{R(\delta_m + 1) - (\delta_{tot} + 1)} \quad (2)$$

where δ_a indicates the particulate depolarization ratio which will be used in all of the following discussion; δ_m indicates the estimated molecular depolarization ratio; $\beta_a^{\perp}$ and $\beta_a^{\parallel}$ indicate the aerosol backscatter signal from the cross-polarized and co-polarized channels, respectively; and R indicates the total aerosol scattering ratio, which is the ratio of the aerosol plus molecular backscatter to the molecular backscatter, including both polarization components.

2.2 Systematic errors

Systematic error can be a concern for depolarization measurements. Potential sources of systematic error in volume depolarization ratio arise in the depolarization optics and calibration. The retrieval of aerosol depolarization ratio can potentially introduce additional systematic error related to the aerosol scattering ratio or uncertainty in the molecular depolarization ratio value. We will provide an overview of the potential systematic errors here, including bounds on the systematic errors for volume depolarization and on the propagated systematic errors for the aerosol depolarization. More details about these potential errors and the means of estimating the error bounds are given in the Appendix.

The volume depolarization ratio, given by Eq. (1), is the more basic measurement. Systematic errors in the volume depolarization can arise from various sources, including calibration errors either in the polarization angle calibration or the gain ratio calibration. A major concern for the measurement of depolarization is the potential for cross-talk, which can arise from a number of sources, including imperfect polarization angle alignment, signal impurities due to imperfections in the polarization beam splitter

ACPD
15, 24751–24803, 2015

(particularly the reflected channel), or other optics, including the aircraft window. Considering these sources, we estimate a reasonable upper bound on the systematic error in the volume depolarization ratio measurement to be 4.7 % (fractional error) in the 355 nm channel, the larger of 5 % fractional error or 0.007 absolute error in the 532 nm channel, and the larger of 2.6 % fractional error or 0.007 absolute error in the 1064 nm channel. Further discussion of these estimates is given in the Appendix.

As can be seen in Eq. (2), the aerosol depolarization ratio, δ_a, depends on the volume depolarization, the molecular depolarization, and the aerosol scattering ratio. Therefore, an error in the assumed value of δ_{mol} or any systematic error in the total scattering ratio, R, can also cause systematic error in the aerosol depolarization ratio. Since the rotational Raman scattering sidebands are completely excluded from the receiver by the narrow-bandwidth background filters, the molecular depolarization arises only from the central Cabannes line and is very well characterized, with a value of 0.0036 (She, 2001; Behrendt and Nakamura, 2002). More critically important is potential systematic error in the total scattering ratio. We estimate the effective upper bound of this error to be 4.1 % in the 532 nm channel from an analysis of the stability of the gain ratio; 5 % in the 355 nm channel including potential errors associated with calibration transfer from the 532 nm channel; and 20 % in the 1064 nm channel taking into account the retrieval of backscatter using an estimated lidar ratio. Again, further discussion can be found in the Appendix.

The estimates given above are intended to be a conservative upper bound on the systematic errors. The systematic errors on the three quantities, δ_{mol}, δ_{tot}, and R, are combined in quadrature using standard propagation of errors for independent variables, as described in the Appendix. The propagated systematic errors for the case studies are included in the figures and tables in Sects. 3 and 4.

ACPD
15, 24751–24803, 2015

3 Dust

In this section we discuss two case studies in which HSRL-2 made three-wavelength measurements of the depolarization of dust.

3.1 Case study: 13 July 2014, dust in the residual layer in North American Midwest

On 13 July 2014, HSRL-2 aboard the B200 made measurements at three wavelengths on a transit flight from Virginia to Colorado for the DISCOVER-AQ field mission (http://discover-aq.larc.nasa.gov/). The aerosol backscatter at three wavelengths and aerosol extinction at two wavelengths are shown in Fig. 3 for a 180 km portion of the flight track in Missouri and Kansas, in the Midwestern United States. Several aerosol layers are evident. For this case study, we will focus on a dust layer that extends from just above the boundary layer to about 3200 m a.s.l. Back-trajectories derived from the NOAA Hybrid Single Particle Lagrangian Integrated Trajectory Model (HYSPLIT) tool (ready.arl.noaa.gov) indicate that this dust layer probably has a Saharan origin and has undergone a very long transport period of about 14 days. Non-spherical particles, such as dust, have a distinct signature in lidar particle depolarization measurements. The particle depolarization ratio measurement curtains for all three wavelengths are shown in Fig. 4. Values of particle depolarization ratio in the 1600–2300 m altitude range are approximately 0.246 ± 0.018 (standard deviation for the sample) $\pm$ (0.055 systematic), $0.304 \pm 0.005 \pm (0.022)$, and $0.270 \pm 0.005 \pm (0.009)$ at 355, 532 nm, and 1064 nm, respectively. These high values of the particle depolarization ratio indicate that the layer is mostly dust (80–90 % dust using the methodology of Sugimoto and Lee, 2006). Note that the particle depolarization ratio at 532 nm for this layer is larger than at either 355 or 1064 nm. The 532 nm layer optical depth is approximately 0.1. The backscatter Ångström exponent (532/1064 nm) is 0.45 ± 0.03 (standard deviation) for this layer. Table 1 includes these values for this sample and for the other cases discussed here. Values for the particle depolarization ratios and backscatter Ångström exponents are

ACPD
15, 24751–24803, 2015

within the interquartile range we previously reported for pure dust measurements from HSRL-1 (Burton et al., 2013).

Figure 5 shows both the aerosol depolarization and volume depolarization measurements for all altitudes at time = 17.2 UT (17:12 UT). The aerosol depolarization ratio random and systematic uncertainties (estimated upper bounds) are also shown.

The predecessor of the HSRL-2, the NASA Langley HSRL-1 instrument, observed several cases of transported Saharan dust in the Caribbean in August 2010, for example the case on 18 August 2010 that is shown by Burton et al. (2012). For that case, the particle depolarization ratios at 532 and 1064 nm are 0.33 ± 0.02 (standard deviation) and 0.28 ± 0.01, slightly higher than the 13 July 2014 case but agreeing within the spread of the measurement sample. The backscatter Ångström exponent (532/1064 nm) is 0.68 ± 0.13 (Table 1). As on 13 July 2014, the particle depolarization ratios and the backscatter Ångström exponent are within the interquartile range of values for pure dust reported for HSRL-1. The backscatter Ångström exponents (532/1064 nm) are larger than the value reported for pure Saharan dust in Morocco (Tesche et al., 2009b), which is 0.28 ± 0.16. The larger values may be consistent with large particle loss during transport, discussed in more detail below.

The particle depolarization spectral dependence can also be compared to measurements of pure dust particle depolarization ratio reported by Freudenthaler et al. (2009) for the Saharan Mineral Dust Experiment (SAMUM I) campaign. For the four dates presented in their Fig. 7, the minimum and maximum values for 355 nm from the Portable Lidar System POLIS were 0.21–0.31 (compare 0.25 for NASA HSRL-2 case); at 532 nm they were 0.29–0.33 from the German Aerospace Center (DLR) HSRL (compare 0.30 and 0.33 from NASA HSRL-2 and HSRL-1) and at 1064 nm they were 0.22–0.29 from the DLR HSRL (compare 0.27 and 0.28 from NASA HSRL-2 and HSRL-1). Again, the reported values at 532 nm exceed those at the other wavelengths. Indeed all three of these case studies, Saharan dust close to the source (Freudenthaler et al., 2009), transported pure Saharan dust observed in the Caribbean by HSRL-1 and trans-

ACPD
15, 24751–24803, 2015

ported Saharan dust observed by HSRL-2 in the Midwestern US, have similar wavelength dependence of the particle depolarization ratio.

3.2 Case study: 8 February 2013, dust in North American Southwest

A less typical observation of pure dust was made by the HSRL-2 instrument on 8 February 2013. On a transit flight to Virginia at the conclusion of the DISCOVER-AQ California field campaign, HSRL-2 aboard the B200 made three-wavelength measurements of a locally produced dust layer very close to the source in the US Southwest. Figure 6 shows the lidar curtain of the aerosol backscatter coefficient at 532 nm for a segment of approximately 280 km in Arizona and New Mexico. The highest backscatter values are near the surface and are associated with the dust layer. More tenuous layers are also visible between 3 and 5 km, which are probably smoke. The discussion will focus primarily on the dust layer for this example. Figure 7 shows particle depolarization ratio at three wavelengths for the same flight segment.

The maximum backscatter values occur within 400 m of the ground at about 17:08 UT (17.14 UT), near the Potrillo volcanic fields in New Mexico in the Chihuahuan Desert. The layer is shallower than the previous case, and the layer AOD is only about 0.02 at 532 nm. The peak particle depolarization ratio is $0.24 \pm 0.05 \pm (0.05)$, $0.37 \pm 0.01 \pm (0.02)$, and $0.383 \pm 0.006 \pm (0.011)$ at 355, 532, and 1064 nm respectively (the first uncertainty value represents standard deviation and parenthesis indicate systematic error bounds). Given that these very large depolarization values occur very close to the ground, we infer that this observation is close to the source region. This observed dust layer is locally generated, wind driven dust from a bare soil surface in desert scrubland. The large particle depolarization ratios provide confidence that this airmass is nearly pure dust and not a mixture. The backscatter Ångström exponent (532/1064 nm) is -0.09 ± 0.04.

Figure 8 shows line plots of the profiles of volume depolarization ratio and aerosol depolarization ratio, plus error bars. The systematic errors are generally larger at 355 nm. This error magnification at 355 nm occurs in both dust cases because of the spectral

ACPD
15, 24751–24803, 2015

dependence of the scattering and consequent small total scattering ratio at 355 nm (TSR = 1.2 at 355 nm). However, the systematic error bounds are small enough to clearly reveal that the wavelength dependence of the particle depolarization ratio is quite different from the Saharan dust cases discussed previously, both those measured by the NASA Langley HSRL-1 and HSRL-2 instruments and by other researchers. In our previous observations of transported Saharan dust, the particle depolarization ratio at 532 nm exceeds the value at 1064 nm, but this case differs in that the 1064 nm particle depolarization ratio slightly exceeds the 532 nm value. The difference is primarily in the 1064 nm value, since the 355 and 532 nm particle depolarization ratios are similar to the Saharan dust cases. However, there was a previous observation by HSRL-1 of windblown North American dust on the slope of the Pico de Orizaba near Veracruz, Mexico on 12 March 2006 (Burton et al., 2014; de Foy et al., 2011) which provides an analogous case for comparison. In this case the particle depolarization ratios are 0.33 ± 0.02 (standard deviation) and 0.40 ± 0.01 at 532 and 1064 nm, respectively, similar to the Chihuahuan desert dust on 8 February 2013, and the backscatter Ångström exponent (532/1064 nm) is -0.9 ± 0.4. Note that these backscatter Ångström exponents are significantly smaller than the transported Saharan dust cases discussed in Sect. 3.1.

3.3 Discussion of spectral dependence of particle depolarization ratio of dust

Figure 9 shows the particle depolarization ratio at all three wavelengths for the four HSRL-1 and HSRL-2 cases discussed so far. The HSRL-2 observations of transported Saharan dust have spectral dependence consistent with the elevated Saharan dust reported by Freudenthaler et al. (2009) for the DLR airborne HSRL and ground-based lidar. However, the NASA HSRL-1 and HSRL-2 observations of North American dust at low altitude close to the source appear to fall into a different category. Although all of the observations discussed here from the NASA HSRL-2 and those of Saharan dust in Africa (Freudenthaler et al., 2009) have particle depolarization ratios at 355 nm that

ACPD
15, 24751–24803, 2015

are less than those at 532 nm, there is a large difference at the longest wavelength, with larger 1064 nm particle depolarization ratios for the local dust cases.

Furthermore, the backscatter Ångström exponents in the Chihuahuan desert observation on 8 February 2013 and on Pico de Orizaba on 12 March 2006 are much smaller compared to 0.45–0.68 for the cases of transported Saharan dust. These smaller values are an indication of larger particle sizes (Sasano and Browell, 1989) (although it must be noted that the backscatter Ångström exponent is also sensitive to other factors besides particle size, such as relative humidity, Su et al., 2008). Maring et al. (2003) shows measured size distributions for dust layers over the Canary Islands and Puerto Rico at different stages of transport, and concluded by modeling of these distributions that a combination of Stokes gravitational settling and an offset upward velocity would explain these observations. According to that model, the volume mean diameter decreases only 20 % after 10 days of atmospheric transport, but 80 % of that change occurs within the first 2 days. In other words, the size distributions for transported dust are similar whether transported long distances or short distances, but even layers transported short distances probably have already lost the largest particles to settling. This model applies to Saharan dust transport, but it raises the possibility that dust size distributions immediately over the source such as the North American dust cases presented here will have some proportion of particles significantly larger than those found in the transported layers.

The spectral dependence of particle depolarization ratio is known to be related to the size of the non-spherical particles (Mishchenko and Sassen, 1998). We infer that the difference in depolarization spectral dependence, and in particular the 1064 nm values, are due to larger particles in the observations of windblown dust close to the surface. Ground-based lidar observations by Ansmann et al. (2009) of convective plumes of dust and sand being lifted from the surface in Morocco included extremely large particle depolarization ratios of 0.50–1.0 at 710 nm. This supports the connection between large particle depolarization ratios at the longer wavelengths and large particles sizes.

ACPD
15, 24751–24803, 2015

However, the long-wavelength values in the current case study are not nearly as extreme, suggesting perhaps that the particle sizes are not as large.

Theoretical treatments to date have shown that it is difficult to quantitatively predict the spectral dependence of the particle depolarization ratio for dust (Gasteiger et al., 2011; Wiegner et al., 2009; Gasteiger and Freudenthaler, 2014). In these previous studies, single particle depolarization calculations tend to be monotonically increasing with wavelength for large particle sizes (Gasteiger et al., 2011) with a more complicated spectral dependence for smaller particles (Gasteiger and Freudenthaler, 2014), which generally supports that the increasing spectral dependence in the North American cases presented here is due to the presence of larger particles. The theoretical calculation of multi-wavelength particle depolarization for more complex distributions of particles has occurred only for limited cases.

For example, Gasteiger et al. (2011) modeled particle depolarization ratio at multiple wavelengths for parameterizations of dust and using size distributions and refractive indices appropriate for SAMUM measurements. For their reference distribution, the modeled particle depolarization ratio reflects a spectral dependence with a peak in the middle of the wavelength range. Calculated values at 355, 532, 710 and 1064 nm were 0.275, 0.306, 0.311, 0.298, consistent with the measurements we report for the Saharan dust cases from the NASA HSRL-1 and HSRL-2. However, for the dust cases in the immediate vicinity of North American sources, the measured maximum shifts to longer wavelengths, and there is no longer agreement with the modeled values at 1064 nm.

4 Smoke

4.1 Case study: 17 July 2014 North American wildfire smoke

Our third three-wavelength case study is an observation of a smoke plume with large particle depolarization ratios measured during the Colorado deployment of the

ACPD
15, 24751–24803, 2015

DISCOVER-AQ field mission on 17 July 2014 at about 8 km altitude. At this time, wildfire smoke from fires in the Pacific Northwest of the United States blanketed much of the region, visible in a composited Moderate Resolution Imaging Spectroradiometer (MODIS) true color image in Fig. 10. (The smoke situation on that day is also discussed in University of Maryland Baltimore County's US Air Quality Smog Blog, see http://alg.umbc.edu/usaq/archives/2014_07.html, accessed 26 February 2015). Figure 11 shows a view of the smoke plume from the B200.

Figures 12 and 13 show HSRL-2 measurements of 532 nm backscatter and three wavelength particle depolarization ratio as time-height curtains and Fig. 14 illustrates a profile at 19.3 UT (19:18 UT) as a line plot with random and systematic error bars. The pictured flight segment began near the Boulder Atmospheric Observatory tall tower north of downtown Denver and proceeded south for about 70 km to Chatfield Park, then turned north again on a parallel track for 135 km to Fort Collins. The layer optical thickness is about 0.05 at 532 nm. This layer was at high altitude near the aircraft, where there is a range dependence of the detected backscattered light (Hair et al., 2008), due to incomplete geometrical overlap between the transmitted beam and the receiver system. For this reason, the aerosol extinction was not retrieved for this layer and the layer optical depth given above is an estimate using the backscatter measurements and an assumed lidar ratio of 70 sr, which is typical for smoke. For this layer, the particle depolarization ratio is greatest at 355 nm, about $0.24 \pm 0.01 \pm (0.02)$ at the southern end of the flight track, and about 0.17–0.22 in the more northern portions. The particle depolarization ratio at 532 nm is as large as $0.09 \pm 0.02 \pm (0.01)$ at the southern end of the flight track and down to about 0.06 at the northern end. Particle depolarization ratio at 1064 nm is about $0.018 \pm 0.002 \pm (0.008)$ throughout the region (parenthesis indicate systematic errors). Note that the wavelength dependence of the particle depolarization is opposite to what was observed for dust on 8 February 2013, in that the smoke plume has significantly larger particle depolarization ratio at the shorter wavelengths. Since this smoke layer has a very high total scattering ratio, the systematic error bounds are relatively small, and it is clear even at the upper bound of potential systematic error

ACPD
15, 24751–24803, 2015

that the 355 nm aerosol depolarization value significantly exceeds the 532 nm value and the 532 nm value significantly exceeds the 1064 nm value.

The pattern of larger particle depolarization ratio at 532 nm compared to 1064 nm has regularly been observed for smoke with the HSRL-1 instrument; indeed the HSRL-1 aerosol classification methodology (Burton et al., 2012) takes advantage of this spectral dependence. One such example is the aged southwest Canadian smoke plume observed on the eastern seaboard of the US on 2 August 2007 that was shown by Burton et al. (2012). For that prior case, the particle depolarization ratios were 0.07 ± 0.01 and 0.019 ± 0.005 at 532 and 1064 nm, respectively. The observation by HSRL-2 is the first time to our knowledge that particle depolarization ratio has been reported for pure smoke at three wavelengths. Note that while the 532 nm particle depolarization ratio for the smoke case is only about 25–30 % of the value for pure dust, the large particle depolarization ratio at 355 nm for the smoke layer is quite comparable to the 355 nm value for dust.

4.2 Discussion of particle depolarization ratio of smoke

Observed particle depolarization ratios for smoke are quite variable. Frequently the 532 nm particle depolarization ratio is observed to be only a few percent at most and often discounted as negligibly close to zero (e.g. Mattis et al., 2003; Müller et al., 2005). For example, small values of about 2–3 % at 532 nm were observed by HSRL-1 in smoke plumes in Mexico City during the Megacity Initiative: Local and Global Research Observations (MILAGRO) field mission described by de Foy et al. (2011). In the published images of HSRL-1 measurements, the smoke plumes are obvious as local minima in the particle depolarization ratio compared to the relatively high ambient values which are due to regional dusty background conditions. However, higher values of particle depolarization ratio at 532 nm of 0.05–0.11 have sometimes been observed in aged smoke layers, as for example 0.07 observed by HSRL-1 on 2 August 2007 noted above (Burton et al., 2012), 0.06–0.11 for transported Canadian smoke reported in Lindenberg, Germany during the Lindenberg Aerosol Characterization Experiment

ACPD
15, 24751–24803, 2015

(LACE) 1998 by Fiebig et al. (2002), 0.06 for transported Siberian smoke observed in Tokyo in 2003 by Murayama et al. (2004) and 0.05 for Alaskan forest fire smoke observed by Sassen and Khvorostyanov (2008) in 2004. Sugimoto et al. (2010) discuss a case in which much higher 532 nm particle depolarization ratios were observed for smoke from a Mongolian forest fire transported to Japan in 2007. The particle depolarization ratios measured for this smoke were 0.12, 0.14 and 0.15 for layers at two different altitudes observed at Nagasaki and Tsukuba.

The causes of depolarization by smoke are not well understood. Two possible explanations are frequently cited in literature: lifting and entrainment of surface soil into the smoke plume and asymmetry of smoke particles themselves.

For example, the smoke observed by Sugimoto et al. (2010) was associated with pyrocumulonimbus and therefore it is inferred that strong convection lifted soil particles from the surface into the smoke plume, explaining the unusually large particle depolarization ratios. Lifting of soil particles is also cited as a possible explanation of the more moderate but still non-negligible particle depolarization ratios reported by Fiebig et al. (2002), since chemical composition analysis of this plume reveals the presence of alumo silicates and iron oxides/hydroxides. However, this explanation is not sufficient in every case. Murayama et al. (2004) discount soil lifting for their observations of depolarizing smoke since no signature of mineral dust is found in a chemical analysis of this plume. Instead, they cite non-sphericity of smoke particle aggregates as the probable cause. Martins et al. (1998) discuss the non-sphericity of smoke particles observed by scanning electron microscope images and an electro-optical aerosol asymmetry analyzer for a variety of smoke types during the Smoke, Clouds, and Radiation – Brazil (SCAR-B) project in 1995. They concluded that most of the non-spherical particles in the observed smoke were chain aggregates of small black carbon particles, and that the non-sphericity tends to increase with the black carbon ratio. Young smoke (< 1 h) is composed of open clusters of high non-sphericity while aged smoke is composed of tighter clusters with lesser non-sphericity. They also point out that flaming fires (high

ACPD
15, 24751–24803, 2015

combustion efficiency) tend to produce more non-spherical particles than smoldering fires.

Referring back to the theoretical calculations of spectral depolarization discussed in Sect. 3.3., Gasteiger and Freudenthaler (2014) show that spectral dependence monotonically decreasing with wavelength would be possible for non-spherical particles approximately the size of the smallest measured wavelength and one-third the size of the longest wavelength, that is, about 355 nm. Therefore, it seems likely that the large particle depolarization ratio at 355 nm in the HSRL-2 case of 17 July 2014 indicates that the cause of the depolarization in this case is non-sphericity of the relatively smaller soot particles themselves, rather than entrained dust particles or ice crystals which would be expected to be larger. Note, these calculations were performed by modeling the non-spherical particles as spheroids, so may be only qualitatively applicable to carbon aggregates.

Theoretical calculations of particle depolarization by aggregates of soot are given by e.g. Sorensen, 2001; Bescond et al., 2013; Kahnert et al., 2012. Calculations for bare carbon aggregates (Sorensen, 2001; Bescond et al., 2013) tend to produce small values of the particle depolarization ratio, much smaller than what was measured in the HSRL-2 case study. However, Kahnert et al. (2012) model the scattering properties of light absorbing carbon (LAC) aggregates embedded in a sulfate shell, and obtain larger values. They use the discrete dipole method to calculate the depolarization ratio of the aggregate particle in the backscatter direction at 304.0, 533.2 and 1010.1 nm. They show that the particle depolarization generally increases with aggregate particle radius and with the volume fraction of LAC in the aggregate. The values also increase with decreasing wavelength for aggregate particle sizes of 400 nm and smaller; but for 500 nm particles, the particle depolarization peaks at the middle wavelength, 533.2 nm. The maximum calculated particle depolarization values for 7 % LAC fraction by volume is 0.08–0.11 for 500 nm particles at 533.2 nm. This is comparable to the 532 nm measurement on 17 July 2014; however, the calculated value at 304.0 nm for the same size and LAC volume fraction is 0.05–0.07, much smaller than the measured value

ACPD
15, 24751–24803, 2015

(at 355 nm) of 0.24. The largest values calculated for the 304.0 nm wavelength are about 0.12–0.21, occurring for the case of 400 nm particle radii and 20 % LAC volume fraction. The full set of theoretical calculations of particle depolarization ratio for 20 % LAC volume fraction are replotted in Fig. 15 for all three wavelengths to highlight the wavelength dependence. Figure 15 also indicates the HSRL-2 observed particle depolarization ratio in the 17 July smoke plume (at 355, 532, and 1064 nm). The calculated particle depolarization ratios are roughly comparable in magnitude to the HSRL-2 measurements for particle sizes in the 400–500 nm range, but the wavelength dependence matches better for smaller particle sizes. LAC volume fraction of 20 % is quite high and may be unrealistic for this smoke layer and the modeled single scattering albedos for 20 % LAC volume fraction, shown by Kahnert et al. (2012), are quite low (below 0.7 at 533.2 nm), indicating exceptionally absorbing particles, so this model is probably not an exact match for the observation in this case. Yet, it is encouraging that an estimate of particle depolarization ratio of the right magnitude can be made by modeling coated soot aggregates. The model results were for a constant fractal dimension of 2.6, structural prefactor of 1.2, and a monomer radius of 25 nm, values chosen to be consistent with the findings for soot aerosol in Mexico City (Adachi and Buseck, 2008). In the HSRL-2 case study, there could be a different fractal dimension, different size monomer component, different coating or a different fraction of soot per aggregate. In addition, the spectral dependence of the refractive index is not well known, and this will have a significant effect on the spectral dependence of the particle depolarization ratio. While the current state of knowledge is not sufficient to perform a retrieval of particle size using the depolarization measurements alone, it is certainly worth noting that the particle depolarization ratio at three wavelengths is sensitive to and contains some information about the particle size of smoke particles, information that may play a role in future microphysical retrievals.

ACPD
15, 24751–24803, 2015

5 Summary and discussion

We have presented three case studies of depolarizing aerosol observed at three wavelengths (355, 532 and 1064 nm) by the NASA airborne HSRL-2 instrument. These three aerosol layers, two dust layers and a smoke layer, each have a different spectral dependence of particle depolarization, but in each case, the 532 and 1064 nm values agree well with prior analogs in the long record of observations by the predecessor instrument, HSRL-1, and with comparable measurements in literature. The first case, transported Saharan dust, has a peak in the spectral dependence of the particle depolarization at 532 nm. This is in accordance with prior measurements of Saharan dust aloft both close to the source and transported to the Caribbean Sea. The second case, also a dust measurement, but near the surface and very close to the source, has a spectral dependence increasing monotonically with wavelength, differing from the previous case primarily at the longest wavelength, 1064 nm. We infer the cause of this difference to be a greater fraction of very large particles due to proximity to the source region; we believe that the largest particles have settled out of the observed Saharan layers but not the locally produced North American dust plumes in this case and a prior HSRL-1 case. Our third case study is of an elevated, transported smoke layer and has spectral depolarization decreasing monotonically with wavelength. Again we infer that the difference in spectral dependence is due to the size of the non-spherical particles, and specifically, that the depolarization in this case is probably attributable to soot aggregates in the smoke.

Microphysical retrievals (Müller et al., 2014) were not available for these HSRL-2 measurement cases, because the current state of these retrievals is limited to spherical particles. However, as suggested by Gasteiger and Freudenthaler (2014) for dust and ash, these observations suggest the possibility that the particle depolarization ratio measurements may aid in retrievals of particle size of non-spherical dust and smoke particles in the future.

ACPD
15, 24751–24803, 2015

More immediately, since the upcoming EarthCARE satellite mission will include a lidar instrument that measures particle depolarization ratio and lidar ratio at 355 nm only, it is valuable to have measurements of the spectral dependence of depolarization for depolarizing aerosol types. These data will help to build the basis for comparing observations from EarthCARE to existing measurements at 532 nm from the CALIPSO satellite. Studying such correspondence is particularly motivated by the desire to identify different aerosol types observed by the EarthCARE satellite. Particle depolarization ratio is hoped to be particularly useful for distinguishing dust and ash from smoke and other aerosol types (Groß et al., 2014; Illingworth et al., 2014), as it already is for CALIPSO (Omar et al., 2009).

However, as illustrated by the case studies presented here, there is not a single consistent spectral dependence of particle depolarization ratio. On the positive side (from the perspective of corresponding CALIPSO and EarthCARE measurements), for pure dust the 355 and 532 nm particle depolarization ratios appear to be fairly consistent even for different particle sizes and may be relatively easily converted. Variation in the 532 and 355 nm particle depolarization ratio for dust is primarily linked to the fraction of dust particles in a sample (Sugimoto et al., 2003) so inferences of dust mixing ratio (e.g. Sugimoto and Lee, 2006; Tesche et al., 2009a; Nishizawa et al., 2011; Burton et al., 2014) may proceed with 355 nm measurements. However, in the case of dust, the 355 nm signal consistently is significantly both smaller and more difficult to measure accurately than the 532 nm signal, and so the signature of dust may be harder to detect from space at 355 nm than at 532 nm for dilute dust mixtures.

On the other hand, the third case study presented here showed that smoke particle depolarization ratio can be significantly larger at 355 nm than at 532 nm, and in fact the particle depolarization ratio at 355 nm for this smoke case was quite comparable to the dust cases. If this is not an isolated case, and this signature proves typical for some types of smoke, the EarthCARE satellite may observe significant particle depolarization in some types of smoke as well as in dust. If this is the case, global observations of smoke depolarization will present an exciting opportunity for improving our understand-

ACPD
15, 24751–24803, 2015

ing of the optical properties of smoke and how they change with age and processing; however, it will also present a challenge. That is, if particle depolarization ratio measurements are made at 355 nm only, a significant particle depolarization ratio signature alone will not be sufficient for the discrimination of dust and smoke from satellite lidar measurements. EarthCARE will also measure lidar ratio at 355 nm; this is related to absorption but has significant variability for smoke (Groß et al., 2014). EarthCARE will not have backscatter or extinction measurements at a second wavelength to give an indicator of particle size. Therefore, in cases where particle depolarization ratio is ambiguous, it seems that smoke and dust may not be easily separable.

Appendix A: Systematic errors

In Sect. 2.2. we provided bounds on the systematic errors in the volume depolarization ratio of 4.7 % (fractional error) in the 355 nm channel, the larger of 5 % fractional error or 0.007 absolute error in the 532 nm channel, and the larger of 2.6 % fractional error or 0.007 absolute error in the 1064 nm channel. For R (total scattering ratio) we estimate the upper bound on the systematic error to be 4.1 % for the 532 nm channel, 5 % for the 355 channel, and 20 % for the 1064 nm channels. Here in the Appendix, we discuss the error sources and estimates of the upper bounds in more detail.

For the volume depolarization, potential sources of systematic errors include an error in the polarization gain ratio calibration or cross-talk between the co-polarized and cross-polarized signals. The polarization gain ratio calibration generally occurs once or twice per flight as described above in Sect. 2.1. The stability of the gain ratio can be assessed by looking at the change between successive calibrations in the same flight. Conservatively choosing the mean difference plus two standard deviations (calculated for all flights with at least two calibrations per flight in the most recent field campaign) as a realistic upper bound on the polarization gain ratio systematic error yields 4.7 % for the 355 nm channel, 5.0 % for the 532 nm channel, and 2.6 % for the 1064 nm chan-

ACPD
15, 24751–24803, 2015

nel. The fractional systematic error from the gain propagates directly to the volume depolarization ratio.

Residual cross-talk is known to occur in polarization lidars, and must be carefully characterized and eliminated as much as possible. A well-known potential source of cross talk occurs in the reflected channel from a polarization beam splitter. However, this system has been designed with extra polarization beam splitters to eliminate that potential concern, as described in Sect. 2.1. and illustrated in Fig. 2. Clear-air studies have found a small residual cross-talk, which appears as a value of the "clear air" volume depolarization that exceeds the theoretical (molecular only) value. As described in Sect. 2.1., the narrow bandwidths in the system completely eliminate the rotational Raman scattering sidebands, and so the molecular depolarization value is known accurately to be 0.0036 (She, 2001; Behrendt and Nakamura, 2002). Since 2006, we have historically measured minimum depolarization values in clear air of approximately 0.0085–0.0135, which we can attribute to a small remaining ellipticity in the optics or stress birefringence in the aircraft window. The cross talk can be modeled as an ellipticity in the polarization (or, alternately, as an error in the polarization angle, leading to the same result).

We start with the polarization Stokes vector (Born and Wolf, 1999)

$$\boldsymbol{S} = \begin{pmatrix} 1 \\ \cos(2\theta)\cos(2\psi) \\ \cos(2\theta)\sin(2\psi) \\ \sin(2\theta) \end{pmatrix} \tag{A1}$$

where the angles θ and ψ represent the ellipticity angle and polarization offset angle, plus the Mueller matrix for a partially depolarizing backward scattering process

ACPD
15, 24751–24803, 2015

(Mishchenko and Hovenier, 1995; Gimmestad, 2008),

$$\hat{\mathbf{M}} = \begin{pmatrix} 1 & 0 & 0 & 0 \\ 0 & 1 - \frac{2\delta_{\text{tot}}}{\delta_{\text{tot}}+1} & 0 & 0 \\ 0 & 0 & \frac{2\delta_{\text{tot}}}{\delta_{\text{tot}}+1} - 1 & 0 \\ 0 & 0 & 0 & \frac{4\delta_{\text{tot}}}{\delta_{\text{tot}}+1} - 1 \end{pmatrix} \tag{A2}$$

Assuming there is a rotation or ellipticity in the transmission, we derive the correction to the measured depolarization to be

$$\delta_{\text{corr}} = \frac{\delta_{\text{meas}} + \chi + \chi\delta_{\text{meas}} - 1}{\chi - \delta_{\text{meas}} + \chi\delta_{\text{meas}} + 1} \tag{A3}$$

where

$$\chi = \cos(2\theta)\cos(2\psi) \tag{A4}$$

The ellipticity and polarization offset angles θ and ψ are treated identically in Eqs. (A3) and (A4), and are generically considered "cross-talk". The subscript "meas" indicates the measured depolarization ratio and "corr" represents the corrected depolarization ratio, assuming the measurement to be affected by cross-talk. Equation (A3) represents a fairly constant shift in the total depolarization ratio approximately equal to the offset between the measured clear air value and the molecular-only depolarization value. An ellipticity angle of 5.8° ($\chi = 0.980$) would explain the error in the depolarization ratio. A partial correction for the cross-talk was implemented in the archived HSRL-2 data (A full correction as in Eq. (A3) will be included in the next version of processed HSRL-2 data). Taking this into account, we include a factor of 0.007 (absolute) due to cross-talk in the estimated volume depolarization error.

An error in the wave plate angle (offset angle calibration) would also affect the volume depolarization ratio according to Eqs. (A3) and (A4), but this effect is much smaller. The

ACPD
15, 24751–24803, 2015

calibration procedure has been carefully designed and used successfully on both the HSRL-1 and HSRL-2 systems since 2006, and the stability of the offset angle is high. Changes indicated during calibrations are at most 0.4° of polarization (0.2° rotation of the half-wave plate) for all channels (assessed, as before, using the mean plus two standard deviations for all flights having multiple calibrations during the latest field mission). Since the offset angle calibration error is much smaller than the inferred ellipticity (0.4° compared to 6°), we do not include angle calibration directly in the systematic error budget.

Note that not only the volume depolarization measurement itself but also the depolarization gain ratio calibration depend on the correct alignment of the calibration waveplates in Fig. 1. The depolarization gain ratio assessment depends on a polarization alignment of 45° during calibration. This effect on the measured gain will be reflected in the stability of the gain ratio, and so is already included in the gain ratio systematic error assessment discussed above.

The calculated aerosol depolarization ratio, δ_a, is additionally affected by any errors in the total scattering ratio, R, in Eq. (2). For 532 nm, the only significant potential systematic error in R is an error in the calibration gain ratio between the aerosol and molecular channels. The stability of this gain ratio was assessed in a similar manner to the offset angle and polarization gain ratios given above. The upper bound on the 532 nm backscatter gain ratio is estimated to be 4.1 % from the mean difference plus two standard deviations for all flights with multiple calibrations in the latest field mission. A systematic error of 4.1 % in the gain ratio propagates directly to a 4.1 % error in R for the 532 nm channel.

The 355 and 1064 nm channels are somewhat more complicated, because it is not possible to calibrate them directly in the same way as 532 nm. The iodine filter for the 532 nm HSRL channel allows for essentially complete separation of the aerosol signal from the total (aerosol plus molecular) signal, but this is not the case for the interferometer used at 355 nm, and the 1064 nm channel has only one total channel with no separation. So for these channels, the calibration is transferred from 532 nm in

ACPD
15, 24751–24803, 2015

a cloud-free region in the free troposphere, as described by Hair et al. (2008). In the calibration transfer region, we do not assume that there is no aerosol, but do look for regions where the aerosol backscatter ratio is small and can be inferred from the value at 532 nm assuming a constant backscatter Ångström exponent. By using a range of reasonable backscatter Ångström exponents, we conservatively estimate an error of 3 % in total scattering ratio for the 355 nm channel. The 1064 nm aerosol backscatter ratio is also affected by the assumption of the lidar ratio to use for separating the aerosol and molecular part; this sensitivity is relatively small for backscatter at 1064 nm, compared to shorter wavelengths or compared to the sensitivity of extinction. Taking these sources into account, we conservatively use 20 % as the upper bound on error on total scattering ratio, R, at 1064 nm.

For the 355 nm channel, the system implements an interferometer to spectrally separate the aerosol and molecular scattering components. The ratio of the aerosol signal in the aerosol-dominated channel to the aerosol signal in the molecular-dominated channel is referred to as the contrast ratio, which needs to be determined to accurately derive the total scattering ratio. For the HSRL-2 system, fairly high contrast ratios of 15–20 are routinely achieved. Our estimate of the error in the contrast ratio definition is usually a few percent but can be up to 20 %. A 20 % error in the contrast ratio for the smoke case presented here would produce an error in the total scattering ratio of less than 4 %. Adding the contrast ratio error, 4 %, and the calibration transfer error, 3 %, in quadrature yields a conservative estimate of the 355 nm total scattering ratio error of 5 %.

The estimates given above are intended to be a conservative upper bound on the systematic errors. The systematic errors on the three quantities, δ_{mol}, δ_{tot}, and R, are independent and, since their actual values within these upper bounds are unknown, they should be treated statistically. We therefore combine the three sources of systematic error in quadrature to assess the potential systematic error in the aerosol depolar-

ACPD
15, 24751–24803, 2015

ization ratio, δ_a. The propagation is described by the following equation:

$$\left(\frac{\Delta\delta_a}{\delta_a}\right)^2 = F_R\left(\frac{\Delta R}{R}\right)^2 + F_{\delta tot}\left(\frac{\Delta\delta_{tot}}{\delta_{tot}}\right)^2 + F_{\delta_m}\left(\frac{\Delta\delta_m}{\delta_m}\right)^2 \quad \text{(A5)}$$

Here, the Δ symbol indicates the systematic error associated with the various quantities and the propagation factors F_x are defined like this:

$$F_x = \left(\frac{x}{\delta_a}\frac{\partial\delta_a}{\partial x}\right)^2 \quad \text{(A6)}$$

The propagation factors are therefore the factors by which the relative error in the aerosol depolarization is magnified with respect to the relative error in the component variables.

These factors vary with total scattering ratio and total depolarization but do not depend on the systematic errors. To illustrate the behavior of the aerosol depolarization ratio systematic error, Table 2 gives the value of aerosol depolarization and its propagated systematic error (as a percent error) for benchmark values of the total scattering ratio and the total and molecular depolarization, plus their estimated systematic errors. It also gives the propagation factors, F_x. From Table 2, it is clear that the propagation factor for the error in the molecular depolarization is always small, the propagation factor for the total depolarization error is typically 1–2, and the propagation factor for the total scattering ratio, F_R, varies significantly with the scattering ratio. F_R is comparable to $F_{\delta_{tot}}$ except when the total scattering ratio is fairly small; in the case of small scattering, it is significantly larger.

Acknowledgements. Funding for this research came from the NASA HQ Science Mission Directorate Radiation Sciences Program and the DISCOVER-AQ project. M. Kahnert acknowledges funding by the Swedish Research Council (*Vetenskapsrådet*) under project 621-2011-3346. The authors also acknowledge the NOAA Air Resources Laboratory (ARL) for the provision of the HYSPLIT transport and dispersion model and READY website (http://www.arl.

ACPD
15, 24751–24803, 2015

noaa.gov/ready.php) used for some of the analysis described in this work. The MODIS images used in Fig. 7 were obtained from the MODIS Adaptive Processing System (MODAPS) archive. Thank you to Rich Hare and Terry Mack of the NASA Langley Engineering Directorate for their exceptional work on the HSRL-2 instrument. The authors are also very grateful to the NASA Langley B200 King Air crew from the California and Colorado deployments: Mike Basnett, Dale Bowser, Les Kagey, Howie Lewis, Scott Sims, Mike Wusk, and Rick Yasky from LaRC and also Kurt Blankenship and Munro Dearing for their dedication in support of HSRL measurements.

References

Adachi, K. and Buseck, P. R.: Internally mixed soot, sulfates, and organic matter in aerosol particles from Mexico City, Atmos. Chem. Phys., 8, 6469–6481, doi:10.5194/acp-8-6469-2008, 2008.

Alvarez, J. M., Vaughan, M. A., Hostetler, C. A., Hunt, W. H., and Winker, D. M.: Calibration Technique for Polarization-Sensitive Lidars, J. Atmos. Ocean. Tech., 23, 683–699, doi:10.1175/jtech1872.1, 2006.

Ansmann, A., Tesche, M., Knippertz, P., Bierwirth, E., Althausen, D., Muller, D., and Schulz, O.: Vertical profiling of convective dust plumes in southern Morocco during SAMUM, Tellus B, 61, 340–353, doi:10.1111/j.1600-0889.2008.00384.x, 2009.

Behrendt, A. and Nakamura, T.: Calculation of the calibration constant of polarization lidar and its dependency on atmospheric temperature, Opt. Express, 10, 805–817, doi:10.1364/OE.10.000805, 2002.

Bescond, A., Yon, J., Girasole, T., Jouen, C., Rozé, C., and Coppalle, A.: Numerical investigation of the possibility to determine the primary particle size of fractal aggregates by measuring light depolarization, J. Quant. Spectrosc. Ra., 126, 130–139, 2013.

Born, M. and Wolf, E.: Principles of Optics: Electromagnetic Theory of Propagation, Interference and Diffraction of Light, Cambridge University Press, 1999.

Burton, S. P., Ferrare, R. A., Hostetler, C. A., Hair, J. W., Rogers, R. R., Obland, M. D., Butler, C. F., Cook, A. L., Harper, D. B., and Froyd, K. D.: Aerosol classification using airborne High Spectral Resolution Lidar measurements – methodology and examples, Atmos. Meas. Tech., 5, 73–98, doi:10.5194/amt-5-73-2012, 2012.

ACPD
15, 24751–24803, 2015

Burton, S. P., Ferrare, R. A., Vaughan, M. A., Omar, A. H., Rogers, R. R., Hostetler, C. A., and Hair, J. W.: Aerosol classification from airborne HSRL and comparisons with the CALIPSO vertical feature mask, Atmos. Meas. Tech., 6, 1397–1412, doi:10.5194/amt-6-1397-2013, 2013.

Burton, S. P., Vaughan, M. A., Ferrare, R. A., and Hostetler, C. A.: Separating mixtures of aerosol types in airborne High Spectral Resolution Lidar data, Atmos. Meas. Tech., 7, 419–436, doi:10.5194/amt-7-419-2014, 2014.

de Foy, B., Burton, S. P., Ferrare, R. A., Hostetler, C. A., Hair, J. W., Wiedinmyer, C., and Molina, L. T.: Aerosol plume transport and transformation in high spectral resolution lidar measurements and WRF-Flexpart simulations during the MILAGRO Field Campaign, Atmos. Chem. Phys., 11, 3543–3563, doi:10.5194/acp-11-3543-2011, 2011.

Fernald, F. G.: Analysis of atmospheric lidar observations – some comments, Appl. Optics, 23, 652–653, 1984.

Fiebig, M., Petzold, A., Wandinger, U., Wendisch, M., Kiemle, C., Stifter, A., Ebert, M., Rother, T., and Leiterer, U.: Optical closure for an aerosol column: method, accuracy, and inferable properties applied to a biomass-burning aerosol and its radiative forcing, J. Geophys. Res., 107, 8130, doi:10.1029/2000jd000192, 2002.

Freudenthaler, V., Esselborn, M., Wiegner, M., Heese, B., Tesche, M., Ansmann, A., Muller, D., Althausen, D., Wirth, M., Fix, A., Ehret, G., Knippertz, P., Toledano, C., Gasteiger, J., Garhammer, M., and Seefeldner, M.: Depolarization ratio profiling at several wavelengths in pure Saharan dust during SAMUM 2006, Tellus B, 61, 165–179, doi:10.1111/j.1600-0889.2008.00396.x, 2009.

Gasteiger, J. and Freudenthaler, V.: Benefit of depolarization ratio at $\lambda = 1064$ nm for the retrieval of the aerosol microphysics from lidar measurements, Atmos. Meas. Tech., 7, 3773–3781, doi:10.5194/amt-7-3773-2014, 2014.

Gasteiger, J., Wiegner, M., Groß, S., Freudenthaler, V., Toledano, C., Tesche, M., and Kandler, K.: Modelling lidar-relevant optical properties of complex mineral dust aerosols, Tellus B, 63, 725–741, doi:10.1111/j.1600-0889.2011.00559.x, 2011.

Gimmestad, G. G.: Reexamination of depolarization in lidar measurements, Appl. Optics, 47, 3795–3802, 2008.

Groß, S., Freudenthaler, V., Wirth, M., and Weinzierl, B.: Towards an aerosol classification scheme for future EarthCARE lidar observations and implications for research needs, Atmos. Sci. Lett., 16, 77–82, doi:10.1002/asl2.524, 2014.

ACPD
15, 24751–24803, 2015

Hair, J. W., Hostetler, C. A., Cook, A. L., Harper, D. B., Ferrare, R. A., Mack, T. L., Welch, W., Izquierdo, L. R., and Hovis, F. E.: Airborne High Spectral Resolution Lidar for profiling aerosol optical properties, Appl. Optics, 47, 6734–6752, doi:10.1364/AO.47.006734, 2008.

Illingworth, A. J., Barker, H. W., Beljaars, A., Ceccaldi, M., Chepfer, H., Cole, J., Delanoë, J., Domenech, C., Donovan, D. P., Fukuda, S., Hirakata, M., Hogan, R. J., Huenerbein, A., Kollias, P., Kubota, T., Nakajima, T., Nakajima, T. Y., Nishizawa, T., Ohno, Y., Okamoto, H., Oki, R., Sato, K., Satoh, M., Shephard, M., Wandinger, U., Wehr, T., and van Zadelhoff, G. J.: THE EARTHCARE SATELLITE: The next step forward in global measurements of clouds, aerosols, precipitation and radiation, B. Am. Meteorol. Soc., doi:10.1175/BAMS-D-12-00227.1, online first, 2014.

Johnson, M. S., Meskhidze, N., and Praju Kiliyanpilakkil, V.: A global comparison of GEOS-Chem-predicted and remotely-sensed mineral dust aerosol optical depth and extinction profiles, Journal of Advances in Modeling Earth Systems, 4, M07001, doi:10.1029/2011MS000109, 2012.

Kahnert, M., Nousiainen, T., Lindqvist, H., and Ebert, M.: Optical properties of light absorbing carbon aggregates mixed with sulfate: assessment of different model geometries for climate forcing calculations, Opt. Express, 20, 10042–10058, doi:10.1364/OE.20.010042, 2012.

Liu, Z., Fairlie, T. D., Uno, I., Huang, J., Wu, D., Omar, A., Kar, J., Vaughan, M., Rogers, R., Winker, D., Trepte, C., Hu, Y., Sun, W., Lin, B., and Cheng, A.: Transpacific transport and evolution of the optical properties of Asian dust, J. Quant. Spectrosc. Ra., 116, 24–33, doi:10.1016/j.jqsrt.2012.11.011, 2013.

Maring, H., Savoie, D. L., Izaguirre, M. A., Custals, L., and Reid, J. S.: Mineral dust aerosol size distribution change during atmospheric transport, J. Geophys. Res.-Atmos., 108, 8592, doi:10.1029/2002jd002536, 2003.

Martins, J. V., Hobbs, P. V., Weiss, R. E., and Artaxo, P.: Sphericity and morphology of smoke particles from biomass burning in Brazil, J. Geophys. Res.-Atmos., 103, 32051–32057, doi:10.1029/98JD01153, 1998.

Mattis, I., Ansmann, A., Wandinger, U., and Müller, D.: Unexpectedly high aerosol load in the free troposphere over central Europe in spring/summer 2003, Geophys. Res. Lett., 30, D2178, doi:10.1029/2003gl018442, 2003.

McGill, M. J., Welton, E. J., Yorks, J. E., and Scott, V. S.: CATS: a new Earth science capability, in: The Earth Observer, NASA Earth Observing System Project Science Office, 4–8, 2012.

ACPD
15, 24751–24803, 2015

Mishchenko, M. I. and Hovenier, J. W.: Depolarization of light backscattered by randomly oriented nonspherical particles, Opt. Lett., 20, 1356–1358, 1995.
Mishchenko, M. I. and Sassen, K.: Depolarization of lidar returns by small ice crystals: an application to contrails, Geophys. Res. Lett., 25, 309–312, 1998.
Müller, D., Mattis, I., Wandinger, U., Ansmann, A., Althausen, D., and Stohl, A.: Raman lidar observations of aged Siberian and Canadian forest fire smoke in the free troposphere over Germany in 2003: microphysical particle characterization, J. Geophys. Res.-Atmos., 110, D17201, doi:10.1029/2004jd005756, 2005.
Müller, D., Hostetler, C. A., Ferrare, R. A., Burton, S. P., Chemyakin, E., Kolgotin, A., Hair, J. W., Cook, A. L., Harper, D. B., Rogers, R. R., Hare, R. W., Cleckner, C. S., Obland, M. D., Tomlinson, J., Berg, L. K., and Schmid, B.: Airborne Multiwavelength High Spectral Resolution Lidar (HSRL-2) observations during TCAP 2012: vertical profiles of optical and microphysical properties of a smoke/urban haze plume over the northeastern coast of the US, Atmos. Meas. Tech., 7, 3487–3496, doi:10.5194/amt-7-3487-2014, 2014.
Murayama, T., Müller, D., Wada, K., Shimizu, A., Sekiguchi, M., and Tsukamoto, T.: Characterization of Asian dust and Siberian smoke with multiwavelength Raman lidar over Tokyo, Japan in spring 2003, Geophys. Res. Lett., 31, L23103, doi:10.1029/2004gl021105, 2004.
Nishizawa, T., Sugimoto, N., Matsui, I., Shimizu, A., and Okamoto, H.: Algorithms to retrieve optical properties of three component aerosols from two-wavelength backscatter and one-wavelength polarization lidar measurements considering nonsphericity of dust, J. Quant. Spectrosc. Ra., 112, 254–267, doi:10.1016/j.jqsrt.2010.06.002, 2011.
Omar, A. H., Winker, D. M., Kittaka, C., Vaughan, M. A., Liu, Z. Y., Hu, Y. X., Trepte, C. R., Rogers, R. R., Ferrare, R. A., Lee, K. P., Kuehn, R. E., and Hostetler, C. A.: The CALIPSO Automated Aerosol Classification and Lidar Ratio Selection Algorithm, J. Atmos. Ocean. Tech., 26, 1994–2014, doi:10.1175/2009jtecha1231.1, 2009.
Rogers, R. R., Hair, J. W., Hostetler, C. A., Ferrare, R. A., Obland, M. D., Cook, A. L., Harper, D. B., Burton, S. P., Shinozuka, Y., McNaughton, C. S., Clarke, A. D., Redemann, J., Russell, P. B., Livingston, J. M., and Kleinman, L. I.: NASA LaRC airborne high spectral resolution lidar aerosol measurements during MILAGRO: observations and validation, Atmos. Chem. Phys., 9, 4811–4826, doi:10.5194/acp-9-4811-2009, 2009.
Rogers, R. R., Hostetler, C. A., Hair, J. W., Ferrare, R. A., Liu, Z., Obland, M. D., Harper, D. B., Cook, A. L., Powell, K. A., Vaughan, M. A., and Winker, D. M.: Assessment of the CALIPSO Lidar 532 nm attenuated backscatter calibration using the NASA LaRC airborne High Spec-

ACPD
15, 24751–24803, 2015

tral Resolution Lidar, Atmos. Chem. Phys., 11, 1295–1311, doi:10.5194/acp-11-1295-2011, 2011.
Rogers, R. R., Vaughan, M. A., Hostetler, C. A., Burton, S. P., Ferrare, R. A., Young, S. A., Hair, J. W., Obland, M. D., Harper, D. B., Cook, A. L., and Winker, D. M.: Looking through the haze: evaluating the CALIPSO level 2 aerosol optical depth using airborne high spectral resolution lidar data, Atmos. Meas. Tech., 7, 4317–4340, doi:10.5194/amt-7-4317-2014, 2014.
Sasano, Y. and Browell, E. V.: Light-scattering characteristics of various aerosol types derived from multiple wavelength lidar observations, Appl. Optics, 28, 1670–1679, 1989.
Sassen, K. and Khvorostyanov, V. I.: Cloud effects from boreal forest fire smoke: evidence for ice nucleation from polarization lidar data and cloud model simulations, Environ. Res. Lett., 3, 025006, doi:10.1088/1748-9326/3/2/025006, 2008.
Scarino, A. J., Obland, M. D., Fast, J. D., Burton, S. P., Ferrare, R. A., Hostetler, C. A., Berg, L. K., Lefer, B., Haman, C., Hair, J. W., Rogers, R. R., Butler, C., Cook, A. L., and Harper, D. B.: Comparison of mixed layer heights from airborne high spectral resolution lidar, ground-based measurements, and the WRF-Chem model during CalNex and CARES, Atmos. Chem. Phys., 14, 5547–5560, doi:10.5194/acp-14-5547-2014, 2014.
She, C.-Y.: Spectral structure of laser light scattering revisited: bandwidths of nonresonant scattering lidars, Appl. Optics, 40, 4875–4884, 2001.
Shipley, S. T., Tracy, D. H., Eloranta, E. W., Trauger, J. T., Sroga, J. T., Roesler, F. L., and Weinman, J. A.: High spectral resolution lidar to measure optical-scattering properties of atmospheric aerosols. 1. Theory and instrumentation, Appl. Optics, 22, 3716–3724, 1983.
Sorensen, C.: Light scattering by fractal aggregates: a review, Aerosol Sci. Tech., 35, 648–687, 2001.
Su, W. Y., Schuster, G. L., Loeb, N. G., Rogers, R. R., Ferrare, R. A., Hostetler, C. A., Hair, J. W., and Obland, M. D.: Aerosol and cloud interaction observed from high spectral resolution lidar data, J. Geophys. Res.-Atmos., 113, D24202, doi:10.1029/2008jd010588, 2008.
Sugimoto, N. and Lee, C. H.: Characteristics of dust aerosols inferred from lidar depolarization measurements at two wavelengths, Appl. Optics, 45, 7468–7474, 2006.
Sugimoto, N., Uno, I., Nishikawa, M., Shimizu, A., Matsui, I., Dong, X., Chen, Y., and Quan, H.: Record heavy Asian dust in Beijing in 2002: observations and model analysis of recent events, Geophys. Res. Lett., 30, 1640, doi:10.1029/2002gl016349, 2003.

ACPD
15, 24751–24803, 2015

Sugimoto, N., Tatarov, B., Shimizu, A., Matsui, I., and Nishizawa, T.: Optical characteristics of forest-fire smoke observed with two-wavelength mie-scattering lidars and a high-spectral-resolution lidar over Japan, SOLA, 6, 93–96, doi:10.2151/sola.2010-024, 2010.

Tesche, M., Ansmann, A., Müller, D., Althausen, D., Engelmann, R., Freudenthaler, V., and Groß, S.: Vertically resolved separation of dust and smoke over Cape Verde using multi-wavelength Raman and polarization lidars during Saharan Mineral Dust Experiment 2008, J. Geophys. Res., 114, D13202, doi:10.1029/2009jd011862, 2009a.

Tesche, M., Ansmann, A., Müller, D., Althausen, D., Mattis, I., Heese, B., Freudenthaler, V., Wiegner, M., Esselborn, M., Pisani, G., and Knippertz, P.: Vertical profiling of Saharan dust with Raman lidars and airborne HSRL in southern Morocco during SAMUM, Tellus B, 61, 144–164, doi:10.1111/j.1600-0889.2008.00390.x, 2009b.

Wiegner, M., Gasteiger, J., Kandler, K., Weinzierl, B., Rasp, K., Esselborn, M., Freudenthaler, V., Heese, B., Toledano, C., Tesche, M., and Althausen, D.: Numerical simulations of optical properties of Saharan dust aerosols with emphasis on lidar applications, Tellus B, 61, 180–194, doi:10.1111/j.1600-0889.2008.00381.x, 2009.

Winker, D. M., Hunt, W. H., and McGill, M. J.: Initial performance assessment of CALIOP, Geophys. Res. Lett., 34, L19803, doi:10.1029/2007gl030135, 2007.

Yang, W., Marshak, A., Kostinski, A. B., and Várnai, T.: Shape-induced gravitational sorting of Saharan dust during transatlantic voyage: evidence from CALIOP lidar depolarization measurements, Geophys. Res. Lett., 40, 3281–3286, doi:10.1002/grl.50603, 2013.

ACPD
15, 24751–24803, 2015

Table 1. Measured properties for specific dust and smoke samples. To obtain these values, samples were taken at specific times and altitudes comprising 400–4500 distinct measurement points. For the dust cases, values were chosen near the peak value of the 532 nm particle depolarization ratio, where it can be inferred that the aerosol is nearly pure dust. The values are reported as mean ± standard deviation for the sample. Systematic error bounds for aerosol depolarization from HSRL-2 are indicated in parentheses.

		Layer AOD (532 nm)	Particle depolarization ratio (1064 nm)	Particle depolarization ratio (532 nm)	Particle depolarization ratio (355 nm) (HSRL-2 only)	Aerosol Backscatter Ångström exponent (532/1064)
Midwest US 13 Jul 2014	transported Saharan dust	0.10	0.270 ± 0.005 (0.009)	0.304 ± 0.005 (0.022)	0.246 ± 0.018 (0.055)	0.46 ± 0.03
Caribbean 18 Aug 2010	transported Saharan dust	0. 25	0.278 ± 0.012	0.327 ± 0.018	–	0.68 ± 0.13
Chihuahuan desert 8 Feb 2013	local North American dust	0.02	0.383 ± 0.006 (0.011)	0.373 ± 0.014 (0.023)	0.243 ± 0.046 (0.045)	−0.09 ± 0.04
Pico de Orizaba 12 Mar 2006	local North American dust	0.31	0.400 ± 0.009	0.334 ± 0.018	–	−0.9 ± 0.4
Denver 17 Jul 2014	smoke	0.05	0.018 ± 0.002 (0.008)	0.093 ± 0.015 (0.012)	0.240 ± 0.010 (0.021)	1.1 ± 0.1
East Coast US 2 Aug 2007	smoke	0.06	0.019 ± 0.005	0.068 ± 0.010	–	0.62 ± 0.25

ACPD
15, 24751–24803, 2015

Table 2. Illustrates the systematic error in aerosol depolarization ratio propagated from the systematic errors in total scattering ratio, volume depolarization ratio, and molecular depolarization ratio. Benchmark values of R (total scattering ratio), δ_{tot} (the volume depolarization ratio) and δ_{mol} (the molecular depolarization ratio) and typical systematic errors are given in the first three columns. Columns 4–6 give the propagation factors, as described in the text. Column 7 gives the resulting aerosol depolarization ratio and systematic error for each benchmark set. Note: percentages given in this table are fractional errors (not depolarization ratio units).

R	δ_{tot}	δ_{m}	F_R	$F_{\delta tot}$	$F_{\delta m}$	δ_{a}
$3.0 \pm 5\,\%$	$0.15 \pm 5\,\%$	$0.0036 \pm 1\,\%$	0.37	1.2	1×10^{-4}	$0.24 \pm 6\,\%$
$3.0 \pm 5\,\%$	$0.05 \pm 5\,\%$	$0.0036 \pm 1\,\%$	0.26	1.1	8×10^{-4}	$0.07 \pm 6\,\%$
$2.0 \pm 5\,\%$	$0.2 \pm 5\,\%$	$0.0036 \pm 1\,\%$	2.2	1.6	3×10^{-4}	$0.49 \pm 10\,\%$
$2.0 \pm 5\,\%$	$0.1 \pm 5\,\%$	$0.0036 \pm 1\,\%$	1.4	1.3	6×10^{-4}	$0.22 \pm 8\,\%$
$2.0 \pm 5\,\%$	$0.05 \pm 5\,\%$	$0.0036 \pm 1\,\%$	1.1	1.2	0.002	$0.10 \pm 8\,\%$
$1.2 \pm 5\,\%$	$0.05 \pm 5\,\%$	$0.0036 \pm 1\,\%$	45	1.9	0.008	$0.37 \pm 34\,\%$

ACPD
15, 24751–24803, 2015

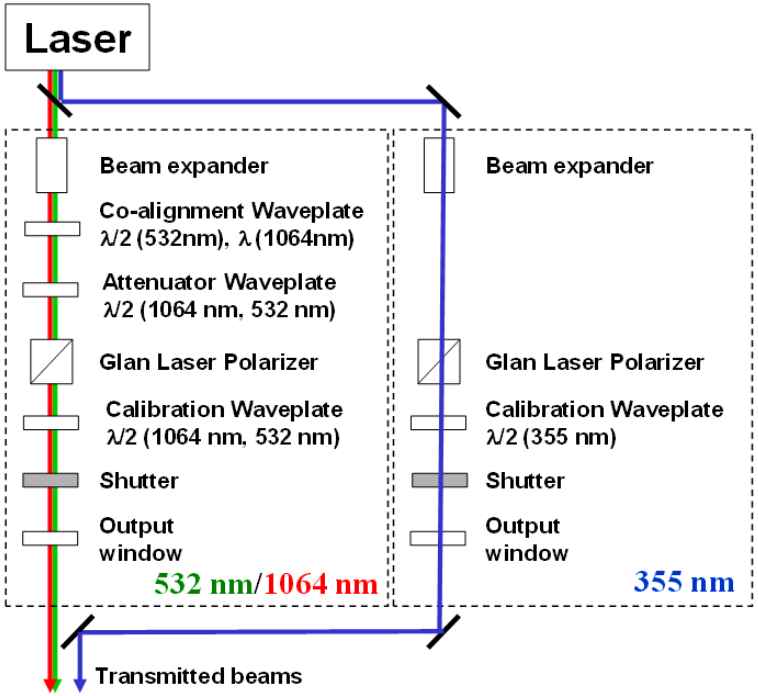

Figure 1. A simplified block diagram of the transmitter optics relevant for depolarization measurements by HSRL-2. The two Glan Laser Polarizers are the primary components ensuring the transmitted laser light is polarized. The motorized Calibration Waveplates are used to align the output polarization to the receiver polarization analyzers. The 532 and 1064 nm laser beams are maintained as a single beam. Since they do not exit the laser at the same polarization, a Co-alignment waveplate is used to align the polarization from the two wavelengths so that the Glan Laser Polarizer does not significantly reduce the amount of light transmitted at one of the wavelengths. The attenuator waveplate is used to attenuate the 532 nm beam for eye safety considerations when flying at low altitudes, and for maximizing the power output otherwise.

ACPD
15, 24751–24803, 2015

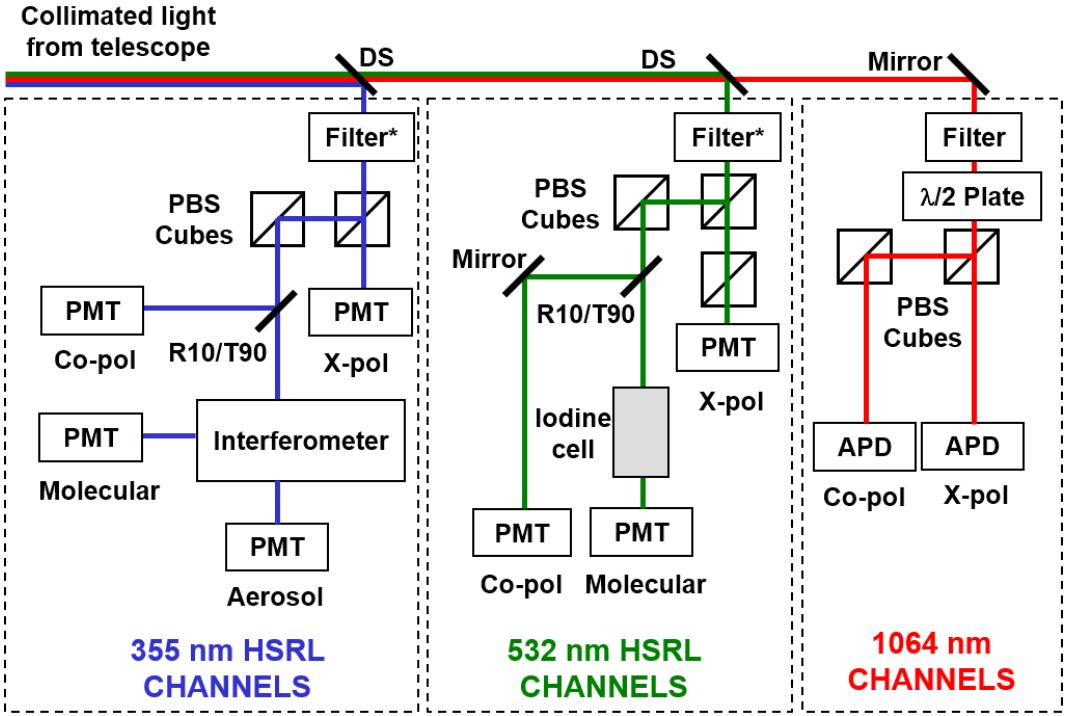

ACPD
15, 24751–24803, 2015

Spectral dependence of particle depolarization using HSRL

S. P. Burton et al.

Figure 2. A simplified block diagram of the receiver optics relevant for depolarization measurements by HSRL-2. Abbreviations: PMT = Photomultiplier Tube; APD = Silicon Avalanche Photo Detector; DS = Dichroic Beam Splitter; PBS = Polarizing Beam Splitter; Co-pol = Co-polarized channel (with respect to the transmitted light); X-pol = Cross-polarized channel. The collimated light arrives from the telescope and is split into the three wavelengths using Dichroic Beam Splitters. The first optical component filters solar background using either an interference filter (indicated "Filter") or an interference filter and etalon in combination (indicated "Filter*"). The 1064 nm channel also includes an additional half-wave plate which can be used to correct any small polarization misalignment in the receiver system since the 532 and 1064 nm beams are transmitted together. This half-wave plate is set during installation and is not rotated during normal operations. The light then passes through Polarization Beam Splitters to be separated into components co-polarized and cross-polarized with respect to the transmitted beam. Since the extinction ratio of the light exiting a PBS is greater in the transmitted direction than in the reflected direction, a second "clean-up" PBS is included for each detector wavelength to further improve the extinction ratio for the co-polarized light. (An extra clean up PBS is also included for the cross-polarized light in the 532 nm channel.) The co-polarized signal and cross-polarized signal are used to determine total depolarization at each wavelength. The 355 and 532 nm co-polarized channels are split again and passed through additional optics to separate the aerosol and molecular signals (see text).

ACPD
15, 24751–24803, 2015

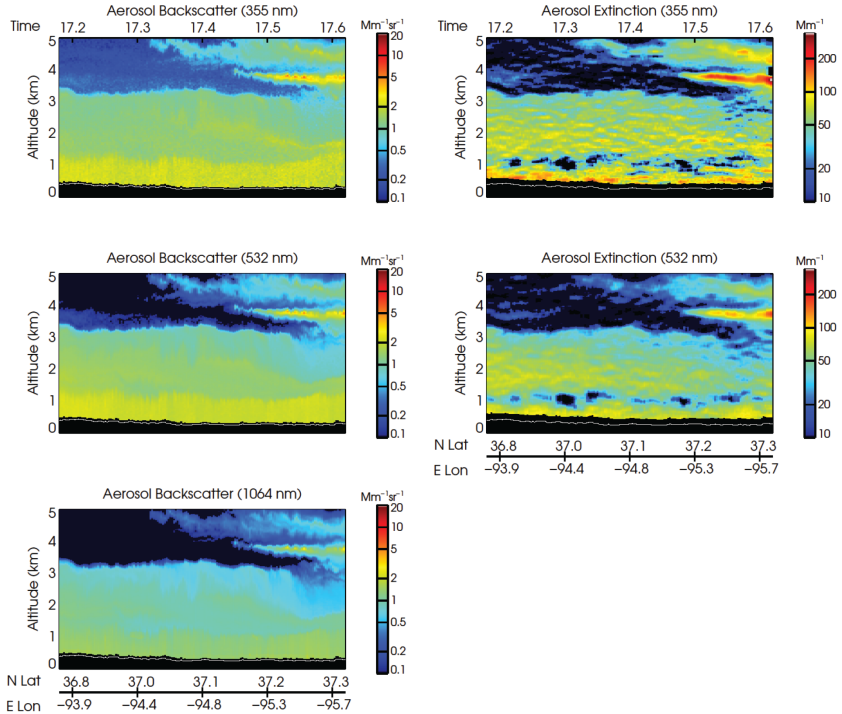

Figure 3. Aerosol backscatter and extinction curtains from HSRL-2 for observations on 13 July 2014 for a flight segment in Missouri and Kansas in the Midwestern United States.

ACPD
15, 24751–24803, 2015

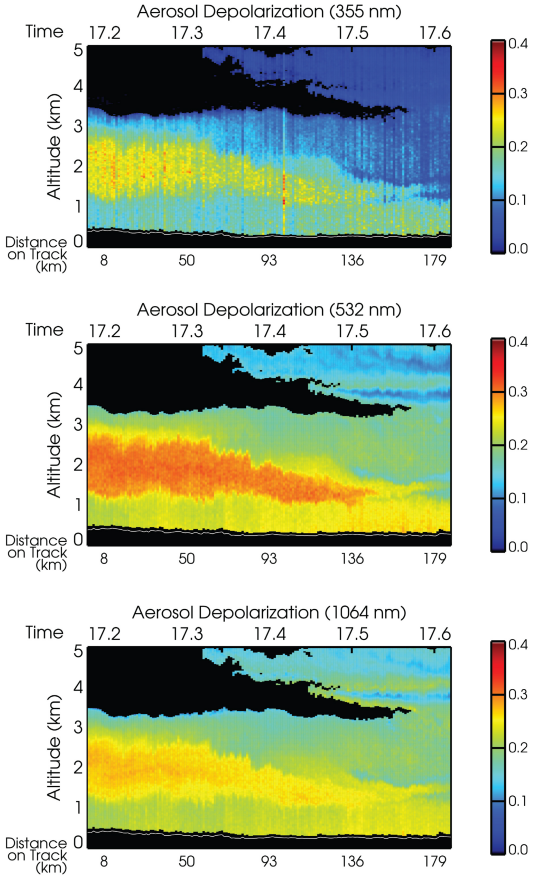

Figure 4. Particle depolarization ratio at three wavelengths measured by the HSRL-2 for the same flight segment shown in Fig. 3.

ACPD
15, 24751–24803, 2015

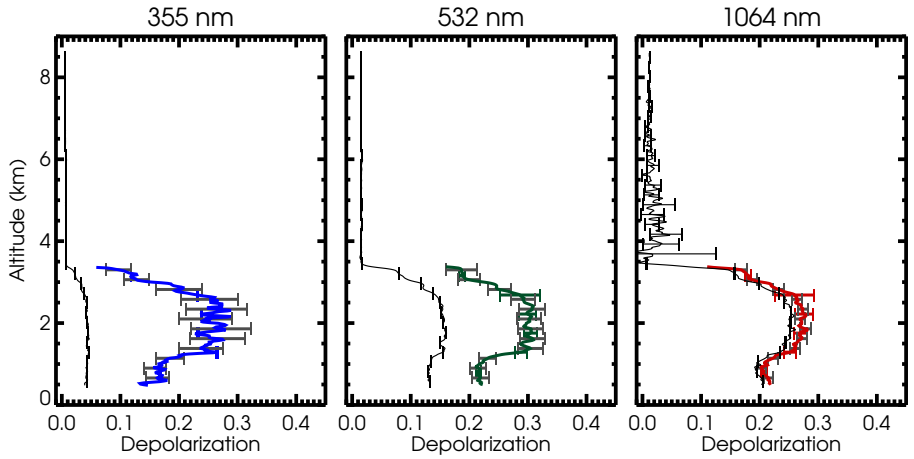

Figure 5. Line plots illustrating the volume and aerosol depolarization ratio profile for the HSRL-2 measurements at 17.2 UT (17:12 UT) on 13 July 2014. The volume depolarization is shown as a thin black line. The error bars on the volume depolarization represent random error (most are small and mostly obscured except 1064 nm). The aerosol depolarization is shown as a thick colored line. Colored error bars indicate random error (most are small enough to be obscured by the line) while gray error bars indicate systematic error bounds, estimated as described in the text. Systematic error bars are not shown for the volume depolarization but see text for estimate. The vertical resolution of these measurements is 30 m and the horizontal resolution is 10 s for all wavelengths.

ACPD
15, 24751–24803, 2015

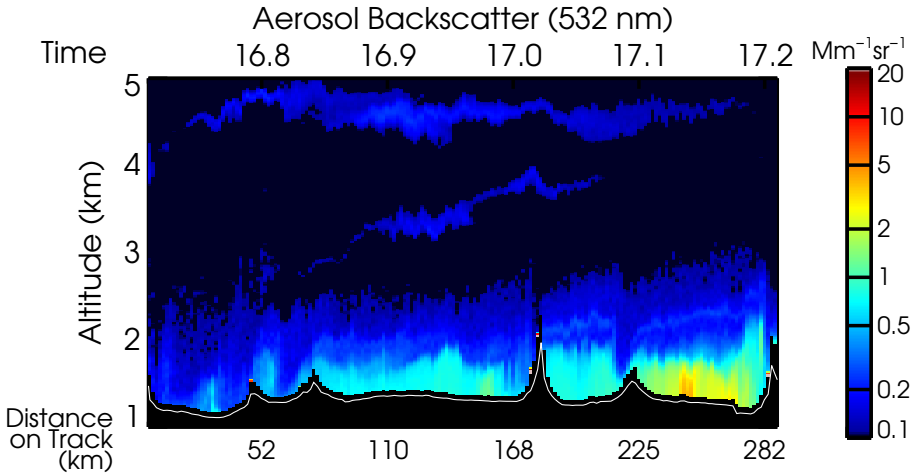

Figure 6. Measurement curtain of aerosol backscatter at 532 nm from the HSRL-2 instrument for a 280 km flight segment over the Southwestern US on 8 February 2013, showing locally generated pure dust in approximately the first kilometer above the surface, as well as very tenuous smoke plumes at higher altitude. This flight segment was part of a transit flight from a field mission in California back to the B200 home base in Virginia. The selected flight segment is approximately 280 km and begins (at the left margin) on the slopes of the Dos Cabezas Mountains of Arizona and ends (at the right margin) at the Franklin Mountains in New Mexico. The ground surface is marked with a white line.

ACPD
15, 24751–24803, 2015

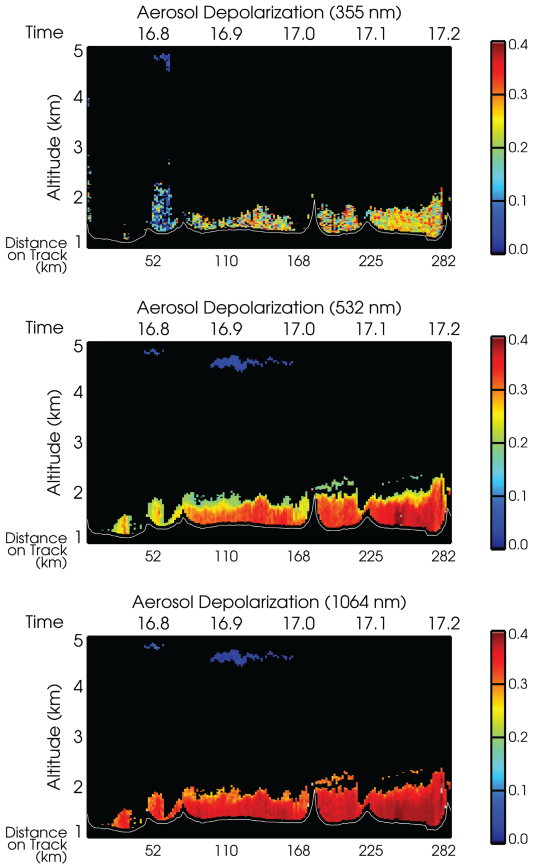

Figure 7. Particle depolarization ratio at three wavelengths observed by HSRL-2 on 8 February 2013 in the Southwestern US for the flight segment shown in Fig. 6.

ACPD
15, 24751–24803, 2015

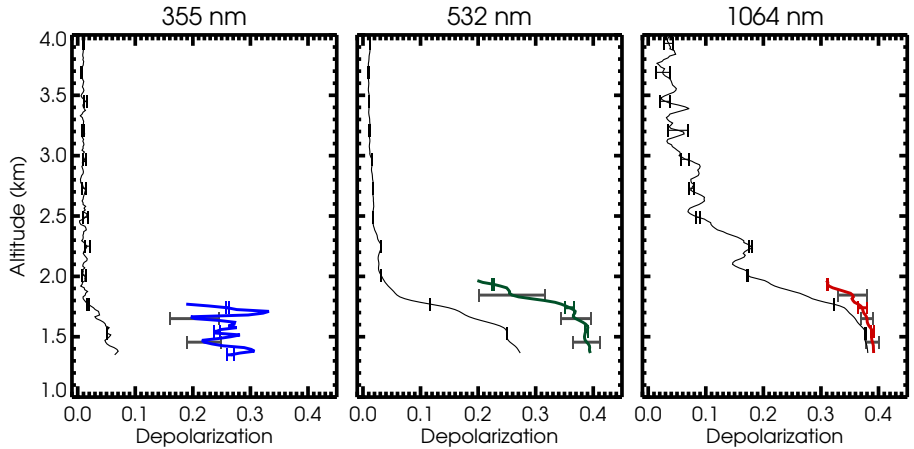

Figure 8. Line plots illustrating the volume and aerosol depolarization ratio profile for the HSRL-2 measurements at 17.14 UT (17:08 UT) on 8 February 2013. Error bars and resolutions as described for Fig. 5.

ACPD
15, 24751–24803, 2015

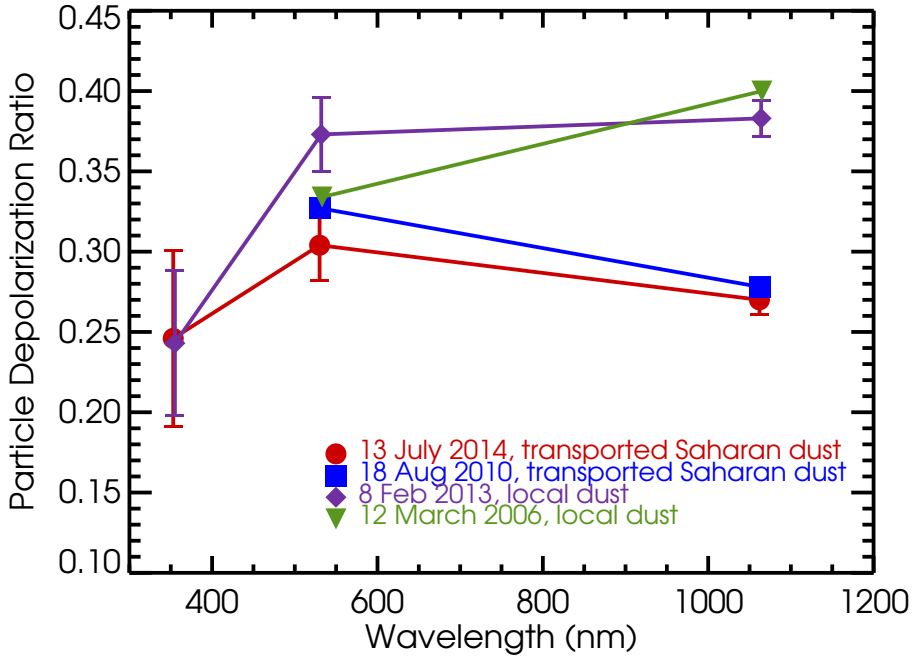

Figure 9. Particle depolarization ratio measured by HSRL-2 and HSRL-1 for the four dust cases discussed in the text. Note the spectral dependence (and in particular the 1064 nm channel) is different for the two local dust cases compared to the transported Saharan dust cases.

ACPD
15, 24751–24803, 2015

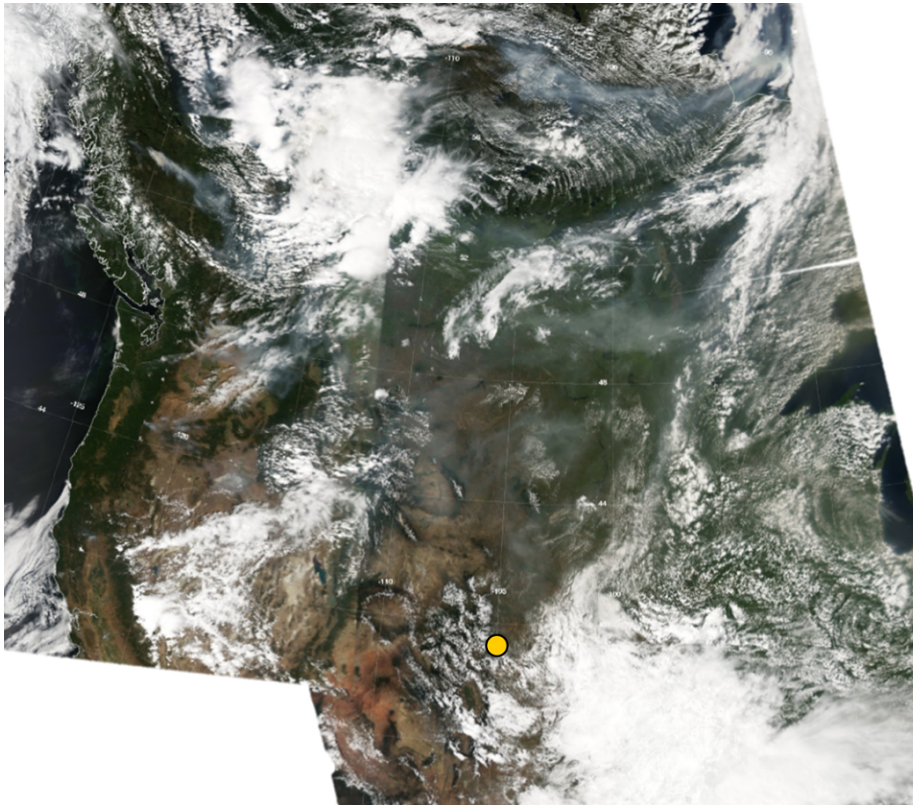

Figure 10. MODIS Aqua true color images of much of North America on 17 July 2014, composited from four granules at 19:45, 19:50, 21:25, and 21:30 UT. Smoke is visible through much of the region. Sources are visible in several places in the US Pacific Northwest and in Western Canada. The approximate location of the HSRL-2 observations discussed in the text (Denver, Colorado) is marked with a yellow dot.

ACPD
15, 24751–24803, 2015

Figure 11. View of the smoke plume aloft on 17 July 2013 taken from the B200. Photo credit: Tim Berkoff.

ACPD
15, 24751–24803, 2015

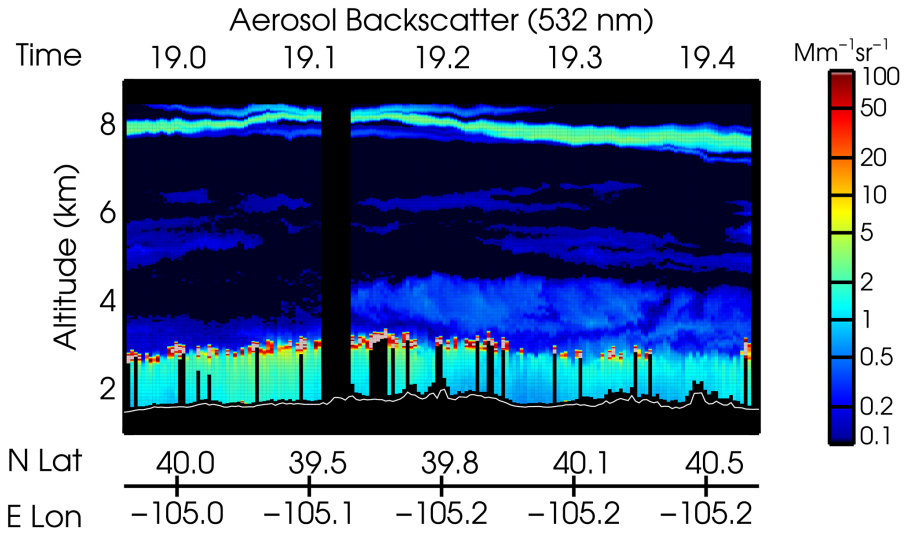

Figure 12. 532 nm aerosol backscatter measurement curtain from HSRL-2 for a portion of a flight on 17 July 2014 in and around Denver, Colorado. Approximately the first third of the pictured curtain is a southbound track between the Boulder Atmospheric Observatory Tall Tower and Chatfield Park, CO. The remainder of the flight is a northbound leg between Chatfield Park and Fort Collins. The blank region indicates a tight turn at Chatfield Park where the lasers were shuttered. Scattered clouds are visible at the top of the boundary layer. Some of these have off-scale backscatter values (tan color) and some are thick enough to cause significant attenuation of the beam; beneath these, data are blanked out due to low signal. The white line indicates underlying terrain. The smoke layer at approximately 8 km is discussed in the text.

ACPD
15, 24751–24803, 2015

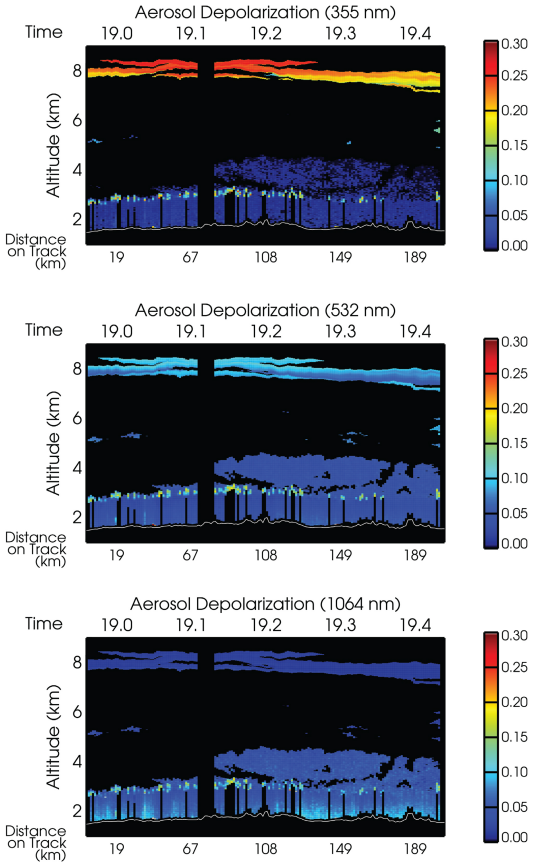

Figure 13. Particle depolarization ratio measurement curtains for the flight segment shown in Fig. 12.

ACPD
15, 24751–24803, 2015

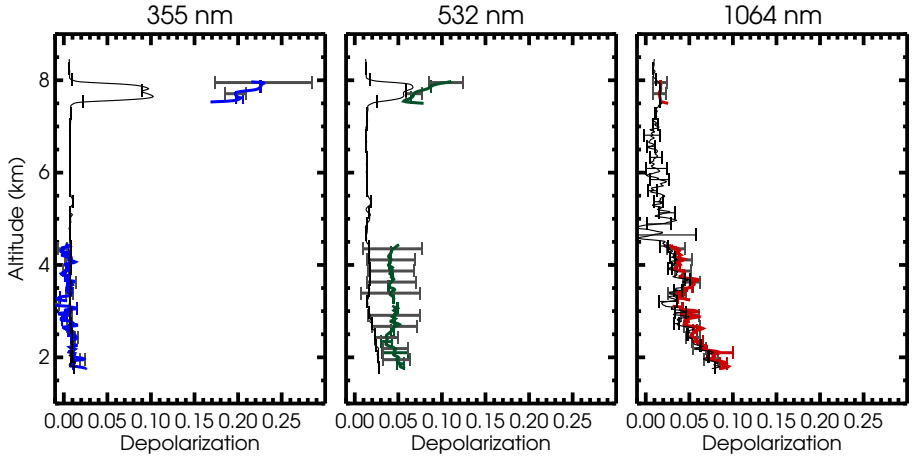

Figure 14. Line plots illustrating the volume and aerosol depolarization ratio profile for the HSRL-2 measurements at 19.3 UT (19:18 UT) on 17 July 2014. Error bars and resolutions as described for Fig. 5.

ACPD
15, 24751–24803, 2015

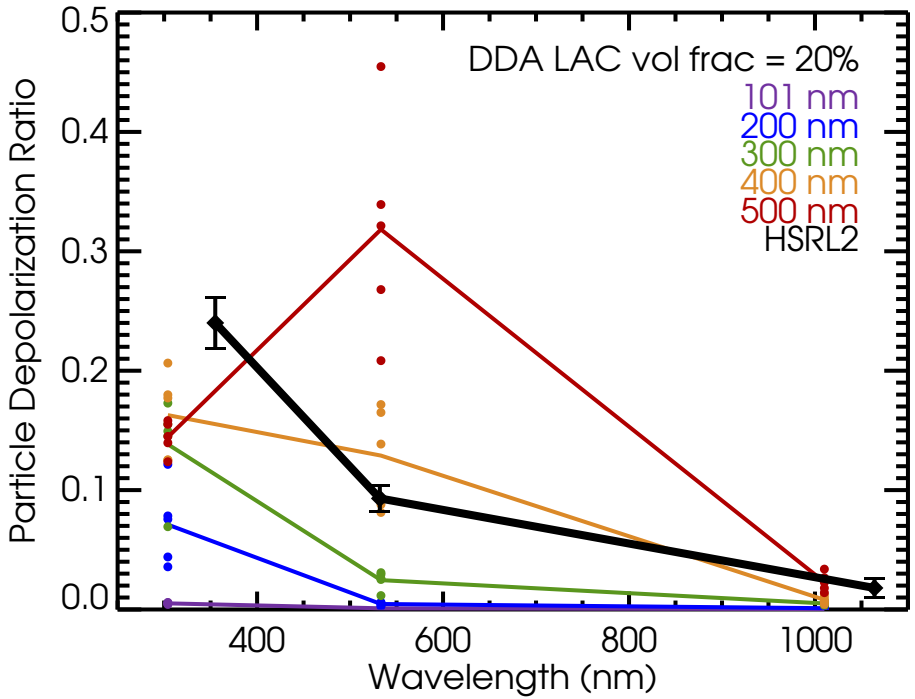

Figure 15. Particle depolarization ratio at three wavelengths for soot aggregates embedded in a sulfate shell reproduced from Kahnert et al. (2012), for 20 % LAC volume fraction. Dots indicate five realizations per aggregate particle size with randomly generated geometries, and the colored lines connect the averages of the five for each wavelength. The legend shows the aggregate particle radii at which the calculation was performed. The thick black line indicates the particle depolarization ratios measured by airborne HSRL-2 within a smoke plume observed on 17 July 2014 at 355, 532, and 1064 nm.

ACPD
15, 24751–24803, 2015